

**Effects of Cloud-Microphysics on Tropical Atmospheric Hydrologic Processes
in the GEOS GCM**

K. M. Lau, H. T. Wu, Y. C. Sud and G. K. Walker

Laboratory for Atmospheres,
NASA, Goddard Space Flight Center

July 2004

(Submitted to J. Climate)

Corresponding author: Dr. K. M. Lau, Laboratory for Atmospheres, Code 910,
NASA/Goddard Space Flight Center, Greenbelt, 20771. Email: lau@climate.gsfc.nasa.gov.

ABSTRACT

The sensitivity of tropical atmospheric hydrologic processes to cloud-microphysics is investigated using the NASA GEOS GCM. Results show that a faster autoconversion rate produces more warm rain and less clouds at all levels. Fewer clouds enhances longwave cooling and reduces shortwave heating in the upper troposphere, while more warm rain produces increased condensation heating in the lower troposphere. This vertical heating differential destabilizes the tropical atmosphere, producing a positive feedback resulting in more rain over the tropics. The feedback is maintained via a two-cell secondary circulation. The lower cell is capped by horizontal divergence and maximum cloud detrainment near the melting/freezing, with rising motion in the warm rain region connected to descending motion in the cold rain region. The upper cell is found above the freezing/melting level, with longwave-induced subsidence in the warm rain and dry regions, coupled to forced ascent in the deep convection region.

The tropical large scale circulation is found to be very sensitive to the radiative-dynamic effects induced by changes in autoconversion rate. Reduced cloud-radiation feedback due to a faster autoconversion rate results in intermittent but more energetic eastward propagating Madden and Julian Oscillations (MJO). Conversely, a slower autoconversion rate, with increased cloud radiation produces MJO's with more realistic westward propagating transients, resembling a supercloud cluster structure. Results suggests that warm rain and associated low and mid level clouds, i.e., *cumulus congestus*, may play a critical role in regulating the time-intervals of deep convections and hence the fundamental time scales of the MJO.

1. Introduction

Recently, there has been a growing body of evidence indicating the importance of tropical warm rain processes in the organization of tropical convection, modulation of clouds and rain types, and possibly global warming. Using three years of data from the Tropical Rainfall Measuring Mission (TRMM), Short and Nakamura (2000) found that more than 20% of the total rain from the tropics is derived from shallow convection. Johnson et al. (1999) showed that approximately 28% of the rainfall during TOGA-COARE may be accounted for by warm rain from mid-level *cumulus congestus*, and pointed to the importance of a mid-tropospheric inversion layer, formed by the melting of ice-phase precipitation falling from above, in limiting the growth of penetrative deep convection. They proposed that a basic trimodal (high, middle, and low), rather than the commonly accepted bimodal (high and low), cloud distribution as a more appropriate description of the tropical cloud system. They also pointed out the importance of the *cumulus congestus* in determining the adjustment time scale of convective cycles. Wu (2003) inferred from theoretical calculations that about 20% of latent heating in the tropics would be contributed by mid-to-low level condensation processes in order to maintain the observed moist static stability profile. Innes et al. (2001) demonstrated that significant improvement in the simulation of the Madden and Julian Oscillation (MJO) can be achieved by increasing vertical resolution that helps to better resolve the melting level in convection in the United Kingdom Meteorological Office's general circulation model (GCM). Li et al. (2001) showed that including cloud-radiation interaction

associated with changes in autoconversion (coalescence–collision processes in warm rain) timescale can lead to a better simulation of the MJO in the Seoul National University GCM. The aforementioned results suggest that warm rain processes are integral components of the tropical convective system. They are also associated with the melting level inversion produced by ice phase processes through melting, freezing, and re-evaporation induced by cumulus updraft and downdrafts. This was further affirmed in Sud and Walker (2003) which showed that including realistic ice-phase processes at the melt/freeze zone can lead to better simulation of low to mid-level convection, and reduce the excessive development of deep convection in early version of McRAS used in the Goddard Earth Observing System (GEOS) GCM.

More recently, Lau and Wu (2003) (hereafter LW) using 3-years of TRMM data, showed that warm rain may be more abundant, and prevalent than all previous estimates. They estimate that it contributes up to 31% of the total rain, and as high as 72% of the total rain area over the tropical oceans. LW also found that for warm rain, mostly associated with middle to low level clouds, there is an increase in rainfall efficiency (defined as the rain production per unit cloud liquid water) of 8-10% per degree C increase in sea surface temperature (SST), whereas for cold rain (associated with ice physics), the rainfall efficiency is virtually independent of SST. They argued that for warm rain, where the large-scale dynamic forcing is weaker, the increasing rainfall efficiency may stem from increased rate of conversion of water vapor to cloud droplets, and to raindrops by diffusion-deposition, and faster growth of raindrops by collision-coalescence. For deep convection, the autoconversion processes are modulated by convective-cloud scale updraft, and hence it is insensitive to surface temperature changes.

LW further hypothesized that in a warmer climate, increased warm rain efficiency may lead to faster rainout of cloud liquid water and consequently lesser amount of water carried upward in deep convection, resulting in overall reduction of clouds at all levels. This paper is aimed at exploring the possible physical underpinnings of such a hypothesis by examining sensitivity of the atmospheric hydrologic cycle to bulk microphysical processes governing the conversion of cloud water substance into precipitation.

2. Model description

The model used is the GEOS GCM Version-2 (GEOS-2), with a $4^\circ \times 5^\circ$ latitude-longitude resolution, and 20 sigma levels with the top of the atmosphere at 10 mb. The model uses the Microphysics of clouds with Relaxed Arakawa-Schubert Scheme (McRAS) developed Sud and Walker (1999a, b). Radiative transfer calculations are based on the shortwave and longwave models of Chou and Suarez (1994), which takes into account the radiative properties of cloud types and its interaction with cloud-microphysics. The most important feature of McRAS germane to the model experiments is the scheme used in the conversion from cloud to rain water which follows Sundqvist (1978, 1988), and adopted in many global climate models, e.g., ECMWF, GSFC, NCEP, LMD, and described in Tiedke (1993), Del Genio et al. (1996) and Sud and Walker (1999a, b) and several others:

$$P = \frac{m}{\tau} [1 - \exp(-(m/m_c)^2)] \quad (1)$$

where m is the cloud water content, m_c the critical cloud water content, and τ the autoconversion (coalescence-collision process) time scale, otherwise referred to as the precipitation time scale. Clearly, Eq (1) expresses the relationship that the

autoconversion rate has an exponential of squared ratio around m_c such that it is negligible if m is much smaller than m_c ; but it quickly approaches its maximum value ($=m/P$) when m exceeds m_c . To account for ice-phase microphysics, including the temperature range in which cloud-ice/cloud-water mixtures coexist, τ and m_c are modified by

$$\tau = \alpha \tau_o F_1 F_2 F_3, \text{ and } m_c = m_{co} / (F_1 F_2 F_3) \quad (2)$$

where α is a scaling parameter for the basic autoconversion time constant τ_o , and m_{co} is the basic critical water content. F_1 , F_2 and F_3 are empirical functions that take into account respectively the dependence of cloud life time and critical cloud water content on the intensity of the coalescence-collision process, coexistence of ice and water droplets (the Bergeron-Findeisen process), and ice-phase physics for high cirrus clouds. In addition McRAS includes cloud dissipation mechanisms associated with cloud top entrainment instability (Del Genio et al. 1996) and diffusive mixing of dry and cloudy air masses within each grid cell and cloud advection. Stratiform clouds are formed by supersaturation produced by either diabatic cooling, or adiabatic cooling associated with the large scale motion. Boundary layer clouds are formed by turbulent eddies carrying saturated water vapor into the highest detraining level below the inversion, following Helfand and Lebraga (1988). The version of McRAS used in this work also includes the latest improvement in ice-phase physics, which allows in-cloud freezing in cumulus updrafts and melting of snowfall below the freezing level (Sud and Walker 2003). The improvement in ice-phase physics has produced more realistic middle level clouds (*cumulus congestus*), consistent with the observed trimodel distribution (Johnson et al. 1999).

As stated previously, LW's results suggest that the autoconversion rate, i.e., warm rain precipitation efficiency, may increase as temperature rises. On the other hand, the indirect effects of aerosols may reduce the autoconversion rate leading to increased cloud life time, and suppressed precipitation (Twomey 1991, Rosenfeld 2002). The suppression of drizzle, in particular, would lead to increased liquid water content in clouds that would enhance the cloud reflectivity and reduced shortwave penetration (Albrecht, 1989). Furthermore, the radiative heating imbalance in the vertical and horizontal, set up by the above processes may lead to redistributions of convection and the large-scale circulation, which in turn modulates the radiative forcings. All these complex processes, whether in response to temperature rise or aerosol increase, appear to hinge on the sensitivity of the radiation-dynamics feedback tied to changes in the autoconversion rate. At present GCMs are incapable of simulating the detailed interaction of cloud microphysics with temperature and aerosols. Yet GCMs with prognostic cloud water use bulk cloud microphysical parameterizations which are related fundamentally to some form of autoconversion process in initiating cloud and rain formation. Thus a study of the sensitivity of cloud-precipitation interaction to the autoconversion process is important in providing some preliminary understanding of possible atmospheric hydrologic responses to global warming and aerosol forcing.

The results presented here are based on sensitivity experiments carried out with different values of the basic autoconversion rate in McRAS. We set $\alpha = 1$ in the control experiment (E0), $\alpha = 0.2$ for fast autoconversion (E1), and $\alpha = 5$ for slow autoconversion (E2). Each experiment was carried out for 5 simulated years (1987-1991) with identical initial conditions starting from January 1, 1987, with observed sea surface temperature

and sea-ice conditions similar to those used for Atmospheric Model Intercomparison Project II. Note that while the autoconversion parameter is defined for warm rain process, a change in the autoconversion rate will be reflected in changes in the entire convective system including warm and cold rain processes as given by Eqs (1) and (2), as well as by induced changes in the large scale circulation. In all the experiments, we use $\tau_o = 10^3$ s, and $m_{co} = 10^{-3}$, and 0.3×10^{-3} kg m⁻³ for convective and stratiform rain respectively. All empirical constants used in the functions F_i 's ($i=1,2,3$) are the same as in Sud and Walker (1999a, b).

3. Results

In this section, results of the control and the anomaly experiments are compared and contrasted to determine the sensitivity of the model climate, organization of convection, and large scale circulation regime to the microphysics of clouds and precipitation.

a. Mean Climate

Fig. 1 shows the comparison of the model climatological annual rainfall and outgoing longwave radiation (OLR) fields for E0 and observations of rainfall from the Global Precipitation Climatology Project (GPCP) (Adler et al. 2003) and OLR from NCEP. Overall the model simulates reasonably well the spatial distribution of both climatologies. However, the model overestimates rainfall, especially over the maritime continent of the western Pacific, and the land regions of northwestern South America and central Africa. It under-develops the ITCZ over the tropical eastern Pacific, and the Atlantic. The similarity in the OLR fields indicates that the model replicates the distribution of deep convections and high cloudiness reasonably well, except, as in the

rainfall case, in the ITCZ regions. The model has higher OLR than observed in the subtropical zones especially over the southeastern tropical Pacific, due to excessive dryness over these regions. Despite the noted biases, the model circulation and rainfall climatologies provide some reassurance to the realism of the model experiments. Further comparison of model results to other relevant observations will be discussed in later sections.

The imposed timescales of autoconversion rates induce fundamental changes in the relationship between cloud liquid water (CLW) and rain rate (RR) in the model climate, as shown in the joint probability distribution function (PDF) of CLW and RR for E0, E1 and E2, shown in Fig. 2. The PDF is constructed based on data from the domain 20°S-20°N, 100°E- 120°W. For observations, data from the Tropical Rainfall Measuring Mission (TRMM) from December 6, 1997 to August 31, 2000 are used. In E0 (Fig. 2c), the presence of two branches in the PDF is obvious. From the slope of the distribution, the upper branch yields a fast cloud life time of about 9-10 minutes, and the lower branch a slow cloud life-time of about 25-30 minutes. The fast branch corresponds to convective scale precipitation, and the slow branch to large-scale stratiform precipitation which is dependent on the ambient relative humidity in the model. The fast branch agrees reasonably well with TRMM observation (Fig. 2a), which has a mean conversion rate of 10-12 minutes, except that the model appears to underestimate the variability about the mean autoconversion rate. The separation of a slow and a fast branch in the model stems from the model's lack of a continuum of processes between convective and stratiform rain. Obviously, for E1 (Fig. 2b), the model accentuates the fast branch yielding a mean cloud life time of about 6 minutes, while eliminating the slow branch

completely. Conversely, for E2 (Fig. 2d), the model tends to favor the slow branch, yielding a range of cloud life timescales that are longer than 20 minutes. Notice a large part of the distributions in E2 has very long cloud life time, indicated by slopes close to zero. The plausible climate and atmospheric hydrologic cycle anomalies introduced by these different precipitation microphysics relationships are examined next.

Fig. 3 shows the spatial distribution of the climatological mean precipitation and OLR for E1 and E2 respectively. In E1, rainfall increases relative to E2 in the maritime continent and northwestern South America, the ITCZ and the South Pacific Convergence Zone (SPCZ) where deep convection prevails. An exception is found in the western North Pacific where E1 shows reduced rainfall relative to E2. This is due to enhanced subsidence in E1 induced by increased ascent from deep convection over the maritime continent. More pronounced is the change in the OLR (Fig. 3b), with E1 showing substantially less areas with OLR less than 220 W/m^2 compared to E2. This is due to the depletion of cloud water by the higher rain-out rate in E1, so that less clouds are found in the middle and upper troposphere. In the zonal mean, the total rainfall reduction (E1 minus E2) is no more than 1 mm/day, with the largest difference occurring mostly in the equatorial region and the southern tropics (Fig. 4a). Note that the differences between the three experiments are comparable to the systematic bias between the model mean and GPCP, which has an inherent uncertainty of 1-1.2 mm/day (Yin et al. 2004). This suggests that even with the large change in autoconversion rate, the total rainfall differences are relatively modest, because of the large-scale redistribution of rainfall. The large change in cloudiness as reflected in the zonal mean OLR is shown in Fig. 4b. There is an approximate 15-25 W/m^2 OLR reduction in the tropics in E2 compared to E1.

Interestingly, E2 agrees with observations better than E1 and E0, and appears to mitigate a negative bias of deep clouds over the equatorial region and the southern tropical oceans compared to observations.

b. Vertical profiles

Fig. 5 shows the vertical profiles of diabatic heating rates: longwave, shortwave, condensation heating and the total heating averaged over the western Pacific warm pool region for E1 (open circle) and E2 (solid square) respectively. Compared to E2, E1 shows increased longwave cooling at all levels up to 250 hPa (Fig. 5a), due to the reduction in cloudiness at all levels (see later discussion for Fig. 6). Reduced upper level cloudiness in E1 also leads to less shortwave absorption by clouds, and hence relative cooling in the upper troposphere above 400 hPa (Fig. 5b). Increased condensation heating is found at all levels in E1, with contributions from both warm and cold condensation (rainout), produced respectively below and above the melting/freezing altitude near 5 km (Fig. 5c). When all the heating terms are combined, the net effect of increased autoconversion rate (E1) is to produce positive total diabatic heating (cooling) below (above) the mean freezing altitude over the warm pool region. Hence we contend that while the direct effect of increased autoconversion is to spur more warm rain, and less cold rain because of rain out of cloud water, cloud-radiative effects could introduce a differential vertical heating that will destabilize the atmospheric column, with a positive feedback leading to further enhanced condensation heating from both warm and cold rain processes. The feedback mechanism is further explored in the following.

The response of clouds, diabatic heating, and large-scale motions are quite different in regions of cold rain (deep clouds), and warm rain (shallow and middle clouds). As

noted in LW, from TRMM data, rain systems having daily rain rate of less than 0.2 mm hr^{-1} with storm heights below the freezing level are considered warm rain. Those with rainrate greater than 2 mm hr^{-1} , and with prevailing storm heights above the freezing altitude are considered cold rain produced primarily by ice-phase precipitation processes. Mixed-phased precipitation produces rain rate between the two thresholds outlined above. The precise thresholds, however, cannot be used here because of the bias in the simulated rainfall intensity. To establish the thresholds, the joint distribution of maximum level of detrainment and daily rain rate has been constructed. The rate of detrainment is computed at all model level as the rate in which moist cloud air is mixed into the environment. The level of maximum detrainment corresponds to the level where cloud dissipation is largest and can be used as a proxy of the maximum storm height.

Figure 6 shows the joint distribution of detrainment height and rain rate for E0. It is clear that for rain rate less than 2 mm day^{-1} , the majority of the rain systems will have cloud tops restricted to below the freezing altitude, (near 500 hPa), and can be considered as warm rain. For rain rate greater than 15 mm day^{-1} , the maximum detrainment heights are well above the freezing altitude. Based on Fig. 6, we shall use the rain rate of 2 mm day^{-1} and 15 mm day^{-1} to define the thresholds for the model warm and cold rain respectively. Consistent with this definition, mixed-phase precipitation, as represented by rain rates falling in between the threshold, has comparable cloud population above and below the freezing level. Using these thresholds, the climatological fractional warm rain in E0 is estimated to be 10% of the total rain amount occupying 70% of the rainy area in the tropics. These numbers are about the same for E1 and E2. For cold rain, the percentages are 53% and 7% respectively. LW showed from TRMM observation the

fractions to be 13%, 63% for warm-rain, and 58% and 7% for cold rain. The agreement between the model and observations is reasonable in view of the uncertainty of observations and simplifying approximations of McRAS.

Having established the model thresholds for warm and cold rain, the vertical profiles of total diabatic heating, cloudiness and vertical motion are computed for each rain type and shown as differences (E1 minus E2) in Figs. 7 and 8. In the warm rain regime (Fig. 7), increased autoconversion leads to an overall reduction in total diabatic heating throughout the atmospheric column due to increased longwave cooling, and reduced shortwave heating (Fig. 7a). The cooling is largest, about $0.4\text{ }^{\circ}\text{C day}^{-1}$ near the surface and reduces towards the lower and middle troposphere, culminating in a positive anomaly in the 900-750 hPa layer. This anomaly is due to condensation heating by the increased warm rain. The diabatic cooling shows a secondary maximum at about 300 hPa. Cloudiness is reduced at all levels, with maximum reduction of 6% near 800 hPa and 4% at 200 hPa (Fig. 7b). The lower peak coincides with the preferred level of warm clouds, and the upper peak with extended anvil clouds in the model cloud climatology (not shown). The warm rain region is dominated by strong subsidence through out the entire troposphere with maximum near 300 hPa (Fig. 7c), consistent with the reduction in cloudiness, and overall diabatic cooling in the region.

Conversely, in the cold rain region (Fig. 8), a faster autoconversion leads to positive net diabatic heating through most of the troposphere with maximum value of $1^{\circ}\text{C day}^{-1}$. This is accompanied by a large reduction of cloudiness below 300 hPa due to increased rain-out of cloud water. As discussed in more detail in the next subsection, a secondary circulation spurred by a precipitation-clouds-radiative feedback leads to

increased deep convection in the cold rain region. This is evident in the increased cloud fraction at 300-200 hPa (Fig. 8b), and anomalous ascending motion up to 30 hPa/day in the upper troposphere (Fig. 8c). The increased ascent in the upper troposphere enhances vertical moisture transport and depletes the moisture in the lower troposphere as well as induces downdraft there. Furthermore, the rain-laden air mass in the lower troposphere loses buoyancy. As a result, there is a large reduction in cloudiness (up to 18%) below 400 hPa (Fig. 8b), and weak net subsidence below 600 hPa (Fig. 8d).

c. Secondary circulations

In this subsection, we present evidence that the anomalous ascent in the cold rain region and descent in the warm rain region are connected via secondary circulations. Fig. 9 shows the differential (E1-minus-E2) vertical mean p-velocity, averaged between 20° S-20° N. The vertical mean is characterized as the general sinking motion over the oceanic warm-rain region attributed primarily to longwave cooling, and induced rising motion concentrated over the cold-rain (deep convection) region of African continent (20-40° E), the maritime continent (100-130° E), and central South America (50-80° W). The secondary motion connecting the warm rain and the cold rain regions can best be seen by calculating the baroclinic component of the vertical motion field, i.e., with the vertical mean component subtracted, for the warm and cold rain regions respectively. In the warm rain region (Fig. 10a), anomalous rising motion is found below the freezing level, and sinking motion with comparable magnitudes (3-6 hPa day⁻¹) above it. The reverse is found in the cold-rain region, but with magnitude of 5-6 time larger (Fig. 10b). The baroclinic vertical motion fields suggest a two-cell secondary circulation. The lower cell is composed of rising motion in the lower troposphere driven by warm rain, capped

by an inversion layer at the freezing level, and a return sinking motion in the cold rain region. The upper cell consists of anomalous rising motion above the freezing level, and forced subsidence below the freezing level. Both cells contribute to large divergence at the freezing level near 500 hPa, where significant cloud detrainment is found.

The secondary circulation is manifested in a warming of the lower troposphere due to increased low level heating by warm rain, and a cooling of the upper troposphere, principally due to longwave radiation, as shown in the height-longitude temperature difference (E1 minus E2) cross-section along the equator in Fig. 11. The vertical temperature distribution is quite uniform across the entire tropics, and is similar for warm and cold rain regions, with the zero line separating the warm and the cold region running near the freezing/melting level. The lower-warm, and upper-cold configuration, leads to an overall destabilization of the tropical atmosphere, providing a positive feedback via the secondary circulation to produce more concentrated, and intense deep convection, reduced cloudiness, but increased warm rain in the middle and lower troposphere.

d. Convective recycling time

In this subsection, we explore the sensitivity of the convective recycling processes to rain microphysics and radiative-dynamic feedback processes. Figures 12 and 13 show the vertical cross-sections of the model condensation heating in different parts of the tropical ocean over a three-month period (1 September, 1988 through 30 November, 1988) for E1 and E2 respectively. During this period, the Indian Ocean is relatively free of deep convection (Figs. 12a, and 13a), while active convection is found over the western Pacific (Figs. 12b, and 13b). In E1, convective activity is more intense and the

time interval between deep convection events appears to be shorter than that of E2, and both low-level and upper level heating are enhanced. In contrast, over the central Pacific (Fig. 12c, and 13c), the intensity and frequency of deep convection are reduced with more low-level heating in E1, indicating a shift to a more warm-rain dominant regime from E2 to E1. As discussed previously, this shift stems from the radiation-dynamic feedback associated with the secondary circulation with enhancing deep convection in the cold rain region, and driving subsidence and limiting the development of deep convection in neighboring regions. Over the eastern Pacific (Figs. 12d and 13d), both E1 and E2 are under the similar climatological large subsidence condition, the increased rainfall efficiency moderately enhanced low-level heating from more warm rains in E1.

To quantify the changes in recycling time of deep convection, we estimate a convective recycling time, as the average time interval between deep convection, defined as convection with substantial condensation heating ($> 4^{\circ} \text{C day}^{-1}$) above 500 hPa. The spatial distribution of convective recycling time is plotted in Fig. 14. It is obvious that in regions of deep convection of the maritime continent and northern South America and central Africa, the recycling time is substantially less in E1 compared to E2. In the deep convective region, the recycling time is less than 7.5–10 days for E1, but generally longer than 10 days in E2. The faster convective recycling time in E1 is due to changes in the moistening processes of the lower troposphere. In E1, the lower and middle troposphere is moistened rapidly because of increased rate of cloud detrainment just below the freezing level (Fig. 15a) compared to E2 (Fig. 15b). As a result, convective available potential energy is rapidly built up as the low and mid level clouds, i.e., *cumulus congestus*, grow and detrain. As shown previously in Fig. 10, the secondary circulation

induced by cloud-radiative feedback produces anomalous uplift in the lower troposphere, favoring the outbreak of convection. A large proportion of the convection is capped by a stable layer at the melting/freezing level. Only a few convective episodes that are stronger will break through to form intense deep convection (see Fig. 15a). The outbreak of convection releases convective instability, and the increased rainfall efficiency leads to a rapid dry out of the lower troposphere. The cycle is repeated with the re-moistening of the lower troposphere by surface fluxes before the next convective outbreak. Hu and Randall (1994) and Lin and Johnson (1996) have proposed a similar mechanism associated with radiative-convective adjustments. Clearly the convective cycling processes are accelerated in E1 compared to E2, shortening the time required for charge and discharge of moisture in the lower troposphere, by detrainment and convection.

e. Intraseasonal Variability

Associated with the changes in recycling of water and associated vertical heating, is a shift in the circulation regime over the tropics between E1 and E2, as illustrated in the daily time-longitude sections of rainfall (Fig. 16) and OLR (Fig. 17). Previous observations (Nakazawa 1988, and Lau et al. 1991) have shown that an MJO can be identified as an eastward propagating supercloud cluster from the Indian Ocean to the central Pacific, embedded by intermittent, transient westward propagating cloud clusters. These features have been attributed to responses of coupled Kelvin (eastward) and Rossby (westward) components to latent heating, modified by air-sea interaction (e.g. Lau and Peng 1987, Wang and Rui 1990, Waliser et al. 1999, and many others). The mix of east-west propagation is reasonably well reproduced in the control E0 (not shown). Figure 16 and 17 emphasize the differences between E1 and E2. In E1 more

intense precipitation and more pronounced eastward propagation associated with the MJO are evident (Fig. 16a). In contrast, in E2 (Fig. 16b), the eastward propagating is less well defined, with more clustering of heavy precipitation events, with accompanying mixed eastward and westward propagations. The difference in supercloud cluster organization is even clearer in daily OLR (Fig. 17). In E1 (Fig. 17a), the OLR signal is not very well defined, and deep convection is more isolated, with contracted cloud anvils. In contrast, in E2 (Fig. 17b), the supercloud cluster structure is more pronounced, with mixed westward propagation embedded in eastward propagating envelopes. The westward propagation of individual cloud streaks, for example is very pronounced during the period from June to August in E2.

Clearly, E1 and E2 represent two distinct circulation regimes excited by cloud-radiative feedback associated with an increase in autoconversion. The overly energetic eastward propagation in E1 is consistent with previous simulations of the MJO in GCM with cumulus parameterization using moisture convergence as closure, but without cloud microphysics influencing the cloud radiative interactions (e.g. Lau and Lau 1986, Slingo et al. 1996, Sperber et al. 2003, Wang and Schlesinger 1999). These GCM simulations tend to produce too fast and too regular eastward propagation modes, and underestimate the supercloud cluster organization, and westward transients. With reduced rainfall efficiency (E2), which enables stronger precipitation-cloud-radiation interaction, the model is able to simulate a more realistic range of tropical intraseasonal variability.

Thus far, the discussions have been focused on the mean and total variability encompassing daily to intraseasonal time scales. The following discussions will be focused on MJO, traditionally defined as the collection of atmospheric features

propagating eastward along the equator from the Indian Ocean to the central Pacific, as seen in broad-band filtered data (Madden and Julian 1972, Lau and Chan, 1985). Fig. 18 shows the 20-70 day variance of rainfall for E1 and E2. In E1, the MJO variances are noticeably enhanced over the climatological convective centers of the maritime continent, eastern Africa and central Americas. In E2, the centers of action of MJO shift to the western and central Pacific around 10° - 20° N, away from the Asian summer monsoon region. This is consistent with the previously described change in rainfall regime, associated with the large scale secondary circulation anomalies (see discussions of Figs. 12 and 13). Figure 19 shows the Hovmöller diagram of 20-70 day band-passed 200 hPa velocity potential for E1 and E2 respectively. During the boreal spring in E1, MJO's, if present, tend to be more energetic and faster with shorter time intervals of 20-30 days between events. At other times, they tend to be relatively less well defined, with each event separated by longer time intervals. In E2, all MJOs are relatively less well defined overall, but they are present all year round. These features are supported by results of an east-west wave spectrum analysis for the entire data period shown in Fig. 20. In E2 (Fig. 20b), a single maximum near 40-day period is found for eastward propagating component, while in E1 a secondary peak with periodicity at 20-30 days can be found, in addition to the 40 day maximum. In both cases, no significant westward propagating signals are detected in the 20-70 day band-passed data.

4. Concluding discussions

From experiments with the GEOS GCM with McRAS, we find that increased autoconversion rate can lead to a substantial change in the atmospheric water cycle

through cloud-radiative-dynamical feedback processes shown in Fig. 21. For fixed sea-surface temperature forcing, a direct effect of increased autoconversion is increased warm rain (non-ice phase) efficiency, associated with more rain and reduced cloudiness at all levels. The reduction in upper level clouds causes increased longwave cooling and reduced shortwave heating, leading to overall cooling and large scale tropical subsidence (indicated by the large downward arrow in Fig. 21). Concomitant with the radiative cooling, which is strongest at the upper levels, is increased low level heating from warm rain, which together maintain a strong vertical heating gradient between the upper and lower troposphere and between the regions of warm rain (low to middle clouds) and cold rain (high clouds). The heating gradient spawns a positive feedback between the region of warm and cold rain, via secondary circulations with rising motion in the lower troposphere and sinking motion in the upper troposphere in the warm rain region, connected to motions of the opposite sign in the cold rain region. In the warm rain region, the secondary circulation provides the uplift energy for buoyant plumes to rise above the lifting condensation level to form clouds, which quickly rainout. As illustrated in Fig. 21, the secondary circulation is characterized by a large-scale divergence at an inversion layer near the melting/freezing level. Large scale descent in the upper troposphere from radiative cooling, and ascent in the lower troposphere from increased warm rain are found in large areas of the tropics. The radiative and condensation heating force ascent in increasing concentrated region of deep convection, with contracted anvil in the upper troposphere, and downdraft in the lower troposphere. Even though the autoconversion processes directly affect warm rain, ice-phase condensation processes play an important role in producing the overall changes in the atmospheric water cycle.

Through cloud-radiation-dynamics feedback, an increase in autocoverion rate will lead to a shorter recycling time for deep convection, which plays a key role in regulating the time scale and intensity of the model MJO. Increased cloud-radiative feedback produces supercloud cluster structure with westward propagating transients, embedded in eastward migrating convection in agreement with observations. The experiments also illustrate the importance of low-to-middle level heating and moistening processes, due to shallow clouds and *cumulus congestus* in determining the slow time scale of the MJO. We find that reduced cloud lifetime, and diminished cloud-radiative feedback caused by excessive rainfall efficiency in E1 leads to more intermittent MJOs, with preferred eastward propagation, but a lack of supercloud cluster structure. These results are in agreement with recent observations and theories of the MJO (Johnson et al. 1999, Raymond 2001, Wu 2003)

An important implication of the present results is that atmospheric hydrologic and dynamical processes may be fundamentally controlled by microphysical processes of clouds and precipitation. Autoconversion is an essential process by which cloud drops grow into rain drops in the initial process of rain formation. While warm rain systems are generally associated with low and middle clouds, even though some eventually grow into deep convection, and precipitate as cold rain through ice-phase precipitation. As suggested by LW, a warmer climate may lead to increased autoconversion and hence affect the redistribution of rain and cloud types, in ways similar to those inferred in this study. Alternatively, autoconversion may be suppressed and cloud lifetime prolonged by increasing anthropogenic aerosols, which act as cloud condensation nuclei, favoring more abundant but smaller cloud droplets (Twomey 1991, Albrecht 1996, and Rosenfeld 2000).

Hence we argue that E1 and E2 in the model experiments may also be viewed as surrogate simulations less or more aerosols in the environment. As an added note, aerosols, both hydrophobic or hydrophilic, can have a significant influence on the vertical distribution of condensation heating as well as the associated direct and indirect effects of clouds on precipitation and cloud-radiative forcing. These are currently introduced into the model based on empirical functions produced with limited observational data. In the real world, the aerosol activation number density affects the cloud droplet production, level of in-cloud supersaturation and even the freezing height of the supercooled cloud-water. These effects will confound our results for comparison with observations. However, we believe these complications will not affect the interpretation of our findings significantly even though some variations at the level of finer details could be necessary.

Most importantly, our results imply that, regardless of whether it is aerosol effects or global warming, microphysical process of precipitation and clouds are the critical pathways by which these effects may regulate the atmospheric water cycle and climate. Increased effort in improving representation of microphysics of precipitation, clouds and aerosols in global climate model is therefore paramount to produce more robust results.

Acknowledgements This work is jointly supported by the Tropical Rainfall Measuring Mission (TRMM) Project, and the Modeling, Analysis and Prediction Program of the NASA Earth Science Enterprise.

Reference

- Albrecht, B., 1989: Aerosols, cloud microphysics, and fractional cloudiness, *Science*, **245**, 1227 - 1230.
- Adler, R. F., G. J. Huffman, A. Chang, R. Ferraro, P. Xie, J. Janowiak, B. Rudolf, U. Schneider, S. Curtis, D. Bolvin, A. Gruber, J. Susskind, and P. Arkin, 2003: The version 2 Global Precipitation Climatology Project (GPCP) monthly precipitation analysis (1979-present). *J. Hydromet.*, **4**, 1147-1167.
- Chou, M.-D., and M. J. Suarez, 1994: An efficient thermal infrared radiation parameterization for use in general circulation models. *NASA Tech. Memo.* 104606, Vol. 3, 85pp. [NTIS N95-15745].
- Del Genio, A. D., N.-S. Yao, W. Kovari, and K. K.-W. Lo, 1996: A prognostic cloud water parameterization for general circulation models. *J. Climate*, **9**, 270-304.
- Helfand, H. M., and J. C. Lebraga, 1988: Design of a nonsingular level 2.5 second-order closure model for prediction of atmospheric turbulence. *J. Atmos. Sci.*, **45**, 113-132.
- Hu, Q., and D. Randall, 1994: Low frequency oscillations in radiative-convective systems. *J. Atmos. Sci.*, **51**, 1089-1099.
- Innes, P. M., J. M. Slingo, S. J. Woolnough, R. B. Neale, and V. D. Pope, 2001: Organization of tropical convection in a GCM with varying vertical resolution: Implication for the simulation of the Madden-Julian Oscillation. *Climate Dynamics*, **17**, 777-793.
- Johnson, R., T. M. Rickenbach, S. A. Rutledge, P. E. Ciesielski and W. H. Schubert, 1999: Trimodal characteristics of tropical convection. *J. Climate*, **12**, 2397-2417.
- Lau, K. M., and H. T. Wu, 2003: Warm rain processes over tropical oceans and climate implications. *Geophys. Res. Lett.*, **30**, 2290-2294.

- Lau K. M., and L. Peng, 1987: Origin of low-frequency (intraseasonal) oscillations in the tropical atmosphere. Part I: Basic theory. *J. Atmos. Sci.*, **44**, 950-972.
- Lau, K. M. and P. H. Chan, 1985: Aspects of the 40-50 day oscillation during northern winter as inferred from outgoing longwave radiation. *Mon. Wea. Rev.*, **113**, 1889-1909.
- Lau, K. M., T. Nakazawa, and C. H. Sui, 1991: Observations of cloud cluster hierarchies over the tropical western Pacific. *J. Geophys. Res.*, **96**, 3197-3208.
- Lau, N.C., and K. M. Lau, 1986: Structure and propagation of intraseasonal oscillations appearing in a GFDL GCM. *J. Atmos. Sci.*, **43**, 2023-2047.
- Li, M. I., I. S. Kang, J. K., Kim, and B. E. Mapes, 2001: Influence of cloud-radiation interaction on simulating tropical intraseasonal oscillation with an atmospheric general circulation model. *J. Geophys. Res.- Atmos.*, **106**, 14219-14233.
- Lin, X, and R. H. Johnson, 1996: Heating, moistening and rainfall over the western Pacific warm pool during TOGA-COARE. *J. Atmos. Sci.*, **53**, 3367-3384.
- Madden, R. and P. Julian, 1972: Description of global scale circulation cells in the tropics with a 40-50 day period. *J. Atmos. Sci.*, **29**, 1109-1123.
- Nakazawa, T., 1988: Tropical super clusters within intraseasonal variations over the western Pacific. *J. Meteor. Soc. Japan*, **66**, 823-839.
- Raymond, D. J., 2001: A new model of the Madden-Julian Oscillation. *J. Atmos. Sci.*, **58**, 2807-2819.
- Rosenfeld, D., 2000: Suppression of rain and snow by urban and industrial air pollution. *Science*, **287**, 1793-1796.

- Short, D., and K. Nakamura, 2000: TRMM radar observations of shallow precipitation over tropical oceans. *J. Climate*, **13**, 4107-4124.
- Slingo, J. M. and AMIP collaborators, 1996: Intraseasonal oscillations in 15 atmospheric general circulation models: results from an AMIP diagnostic subproject. *Climate Dynamics*, **12**, 325-357.
- Sperber, K. R., 2003: Propagation and the vertical structure of the Madden-Julian Oscillation. *Mon. Wea. Rev.*, **131**, 3018-3037.
- Sud, Y., and G. Walker, 1999a: Microphysics of clouds with the relaxed Arakawa-Schubert Scheme (McRAS). Part I: Design and Evaluation with GATE Phase III data. *J. Atmos. Sci.*, **56**, 3196-3220.
- Sud, Y. C., and G. K. Walker, 1999b: Microphysics of clouds with relaxed Arakawa-Schubert Scheme (McRAS). Part II: Implementation and performance in GEOS 2 GCM. *J. Atmos. Sci.* **56**, 3121-3240.
- Sud, Y. C., and G. K. Walker, 2003: Influence of ice-phase physics of hydrometeors on moist convection. *Geophys. Res. Lett.* **30**, 14, 1758-1761.
- Sundqvist, H., 1988: Parameterization of condensation and associated clouds in models for weather prediction and general circulation simulation. In *Physical Based Modeling and Simulation of Climate and Climate Change*, M. E. Schlesinger, Ed. Reidel, 433-461.
- Sundqvist, H., 1978: A parameterization of non-convective condensation including prediction of cloud water content. *Quart. J. Roy. Meteor. Soc.*, **104**, 677-690.
- Tiedtke, M., 1993: Representation of clouds in large scale models. *Mon. Wea. Rev.*, **121**, 3040-3061.

- Twomey, S. A., 1991: Aerosol, clouds and radiation. *Atmos. Environ., Part A*, 25, 2435-2442.
- Waliser, D. E., K. M. Lau, and J. H. Kim, 1999: The Influence of Coupled Sea Surface Temperatures on the Madden-Julian Oscillation: A Model Perturbation Experiment. *J. Atmos. Sci.*, **56**, 333-358
- Wang, B., and Rui, H., 1990: Dynamics of the coupled moist Kelvin-Rossby wave on an equatorial β -plane, *J. Atmos. Sci.*, **47**, 397-413.
- Wang, W., and M. E. Schlesinger, 1999: The dependence on convection parameterization of the tropical intraseasonal oscillation simulated by the UIUC 11-layer atmospheric GCM. *J. Climate*, **12**, 1424-1457.
- Wu, Zhaohua, 2003: A shallow CISK, deep equilibrium mechanism for the interaction between large-scale convection and circulation in the tropics. *J. Atmos. Sci.*, 60 , 377-392.
- Yin, X., A. Gruber, and P. Arkin, 2004: Comparison of the GPCP and CMAP merged gauge-satellite monthly precipitation products for the period 1979-2001. *J. Hydromet.*, **in press**.

Figure Captions

Figure 1 Observed and model annual mean 5-year climatology of a) rainfall and b) OLR.

Rainrate greater than 6 mm/day, and OLR less than $240 \text{ Wm}^{-2}\text{a}$ are shaded.

Figure 2 Joint PDF of rain rate (mm hour^{-1}) and cloud liquid water (mm) from a) TRMM data,

b) E1, c) E0, and d) E2. The PDF is constructed for data within 20°S - 20°N , 100°E - 120°

W.

Figure 3 As in Fig. 1, except for climatology of a) rainfall, and b) OLR of E1 and E2.

Figure 4 Latitudinal distribution of zonal mean of a) rainfall and b) OLR for E0, E1, E2 and

observations, denoted by symbols as shown.

Figure 5 Vertical profile of components of diabatic heating averaged over the warm pool region

(100 - 160°E , 12°S - 12°N) for a) longwave radiation, b) shortwave radiation, c) moist

processes including convective and large scale rain, and d) total diabatic heating). Open

circles are for E1, and solid squares for E2. Units are in $^\circ \text{K/day}$.

Figure 6 Joint distribution of maximum detrainment level and rain rate for E0. Warm-rain and

cold- rain, and mixed-phase regions are as shown. Contours are population counts in natural logarithm scale.

Figure 7 Vertical profile of E1-minus-E2 difference in Q, total heating (K/day); Cl, cloudiness

(percentage), and W, vertical velocity (negative hPa/day) for warm rain.

Figure 8 Same as in Fig. 6, except for cold rain.

Figure 9 Longitudinal distribution of E1-minus-E2 difference in vertical mean p-velocity

(negative hPa/day) averaged over 20°S - 20°N along the equator.

Figure 10 Height-longitude cross-section of E1-minus-E2 vertical velocity (negative hPa/day) averaged over 20° S - 20° N for a) the warm rain region, and b) the cold rain region. Vertical mean value has been subtracted.

Figure 11 Height-longitude distribution of E1-minus-E2 temperature difference averaged over 20° S - 20° N. Units in °K. Vertical mean has been subtracted, and warm anomalies are shaded.

Figure 12 Height-time cross-sections of condensation heating over a) Indian ocean , b) western Pacific, c) central Pacific, and d) eastern Pacific for E1. Contours with heating greater than 1 °K/day and 4° K/day are shaded.

Figure 13 Same as in Fig. 12, except for E2.

Figure 14 Spatial distribution of recycling time of deep convection for a) E1 and b) E2. Unit is in days. Areas with recycling time less than 15 and 10 days are shaded.

Figure 15 Height-time cross-section of detrainment rate over the western Pacific for a) E1 and b) E2. Areas with detrainment rate greater than 2 and 4 kg/sec are shaded.

Figure 16 Time-longitude section of daily precipitation averaged along the equator (8° S - 8° N) for a) E1 and b) E2. Unit is in mm/day.

Figure 17 Same as in Fig. 16, except for OLR. Unit is in Wm^{-2} .

Figure 18 Spatial distribution of standard deviation of 20-70 day filtered precipitation for a) E1 and b) E2. Rain rates greater than 3 mm/day are shaded from light to dark.

Figure 19 Time-longitude section of 20-70 day filtered 200 hPa velocity potential for a) E1 and b) E2. Units are in $10^6 \text{ m}^2 \text{ s}^{-1}$.

Figure 20 East-west wavenumber spectrum of 20-70 day filtered 200 hPa velocity potential for a) E1 and b) E2.

Figure 21 Schematic showing model predicted changes in the atmospheric hydrologic cycle, and cloud-radiative-dynamic feedbacks in the tropics due to increased autoconversion processes.

Figure 1 Observed and model annual mean 5-year climatology of a) rainfall and b) OLR.

Rainrate greater than 6 mm/day, and OLR less than $240 \text{ Wm}^{-2}\text{a}$ are shaded.

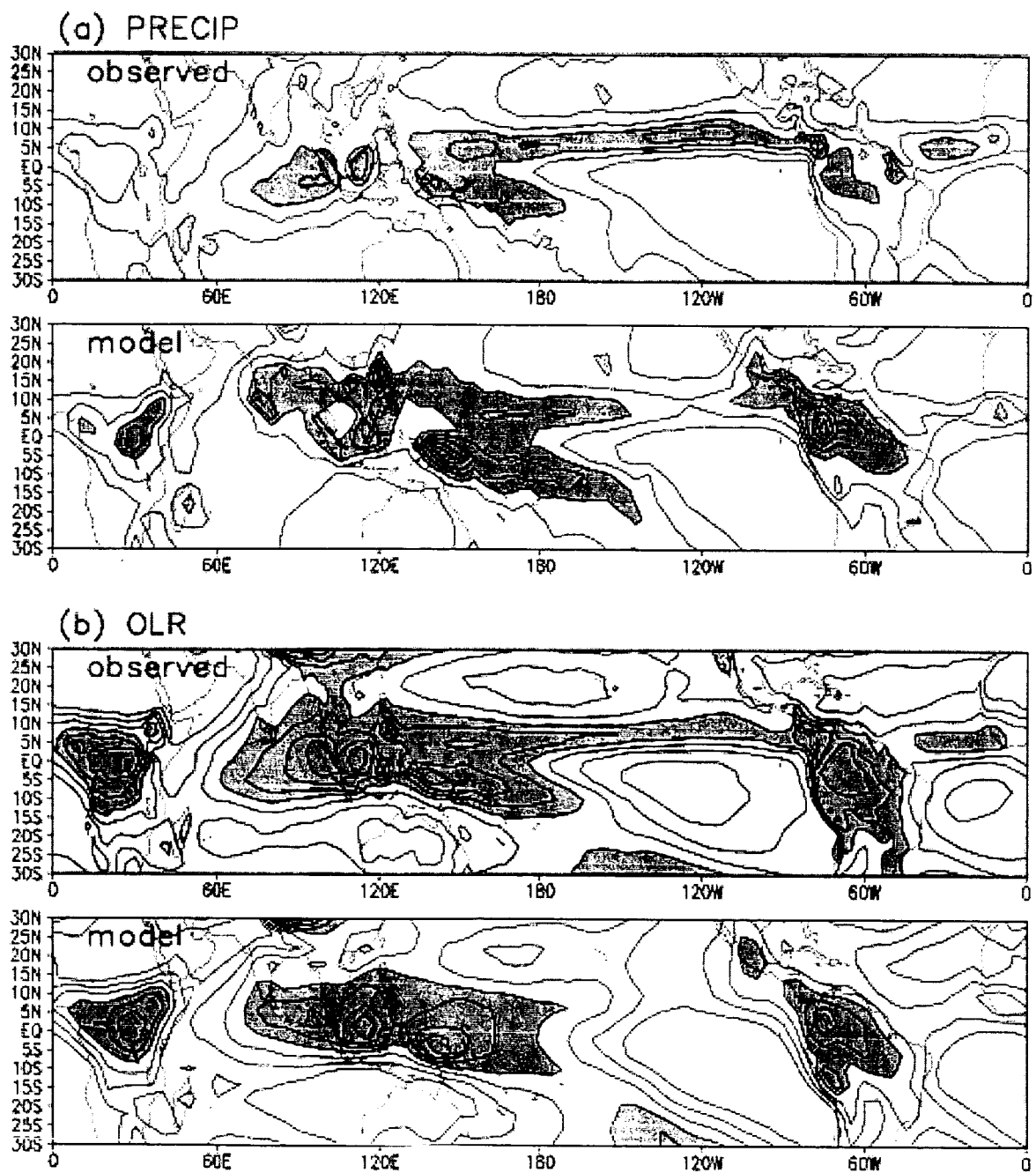


Figure 2 Joint PDF of rain rate (mm hour^{-1}) and cloud liquid water (mm) from a) TRMM data, b) E1, c) E0, and d) E2. The PDF is constructed for data within 20° S - 20° N , 100° E - 120° W .

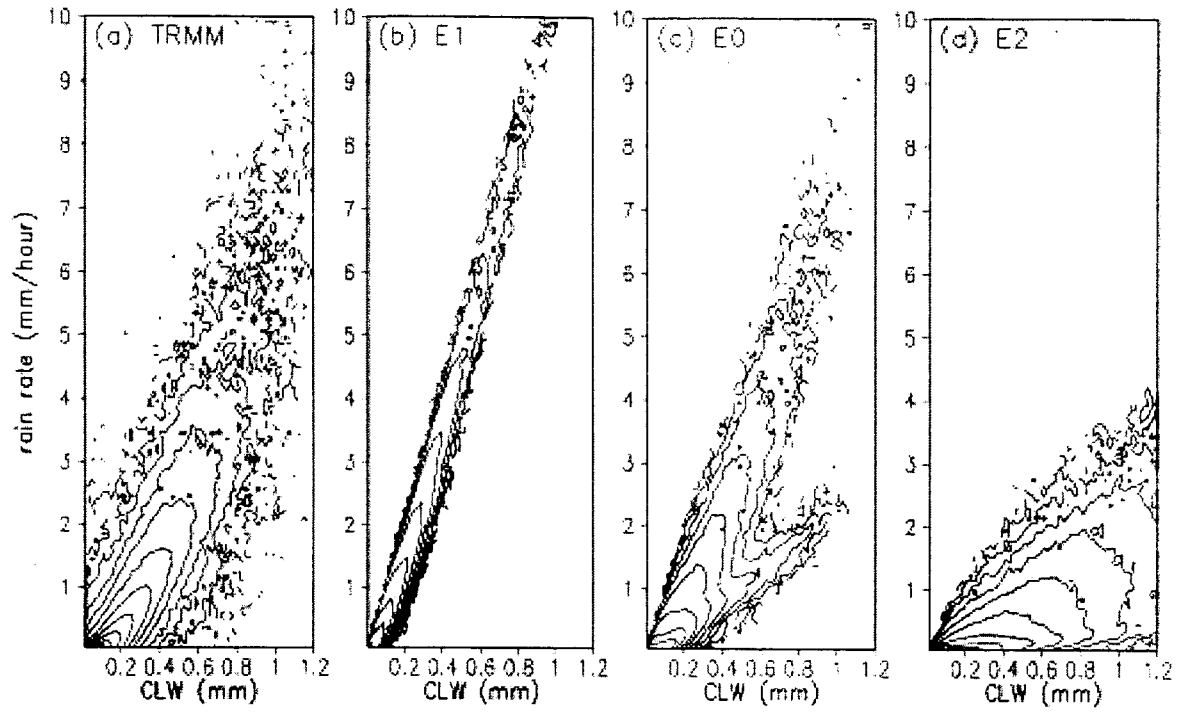


Figure 3 As in Fig. 1, except for climatology of a) rainfall, and b) OLR of E1 and E2.

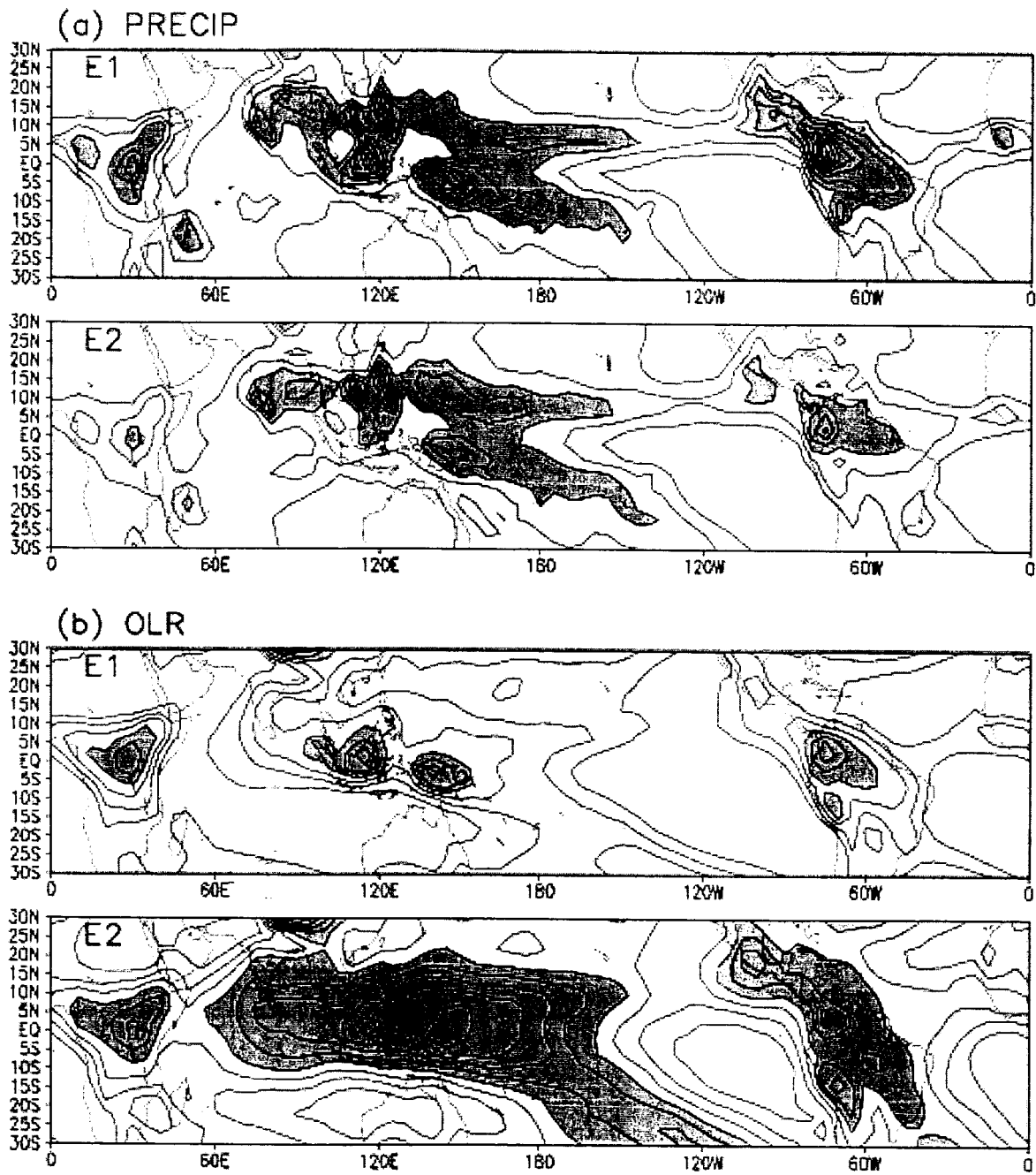


Figure 4 Latitudinal distribution of zonal mean of a) rainfall and b) OLR for E0, E1, E2 and observations, denoted by symbols as shown.

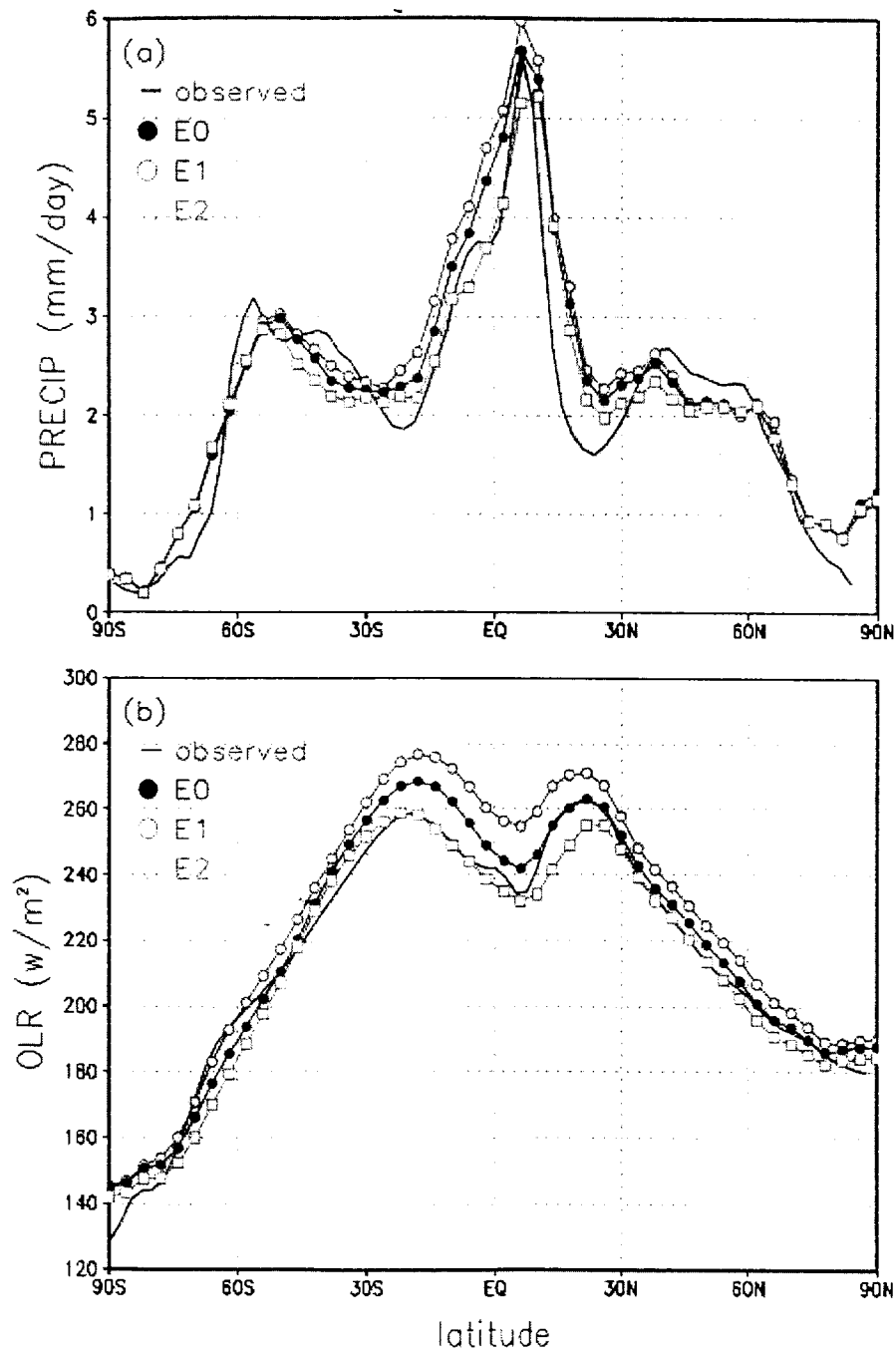


Figure 5 Vertical profile of components of diabatic heating averaged over the warm pool region (100-160°E, 12°S-12°N) for a) longwave radiation, b) shortwave radiation, c) moist processes including convective and large scale rain, and d) total diabatic heating). Open circles are for E1, and solid squares for E2. Units are in ° K/day.

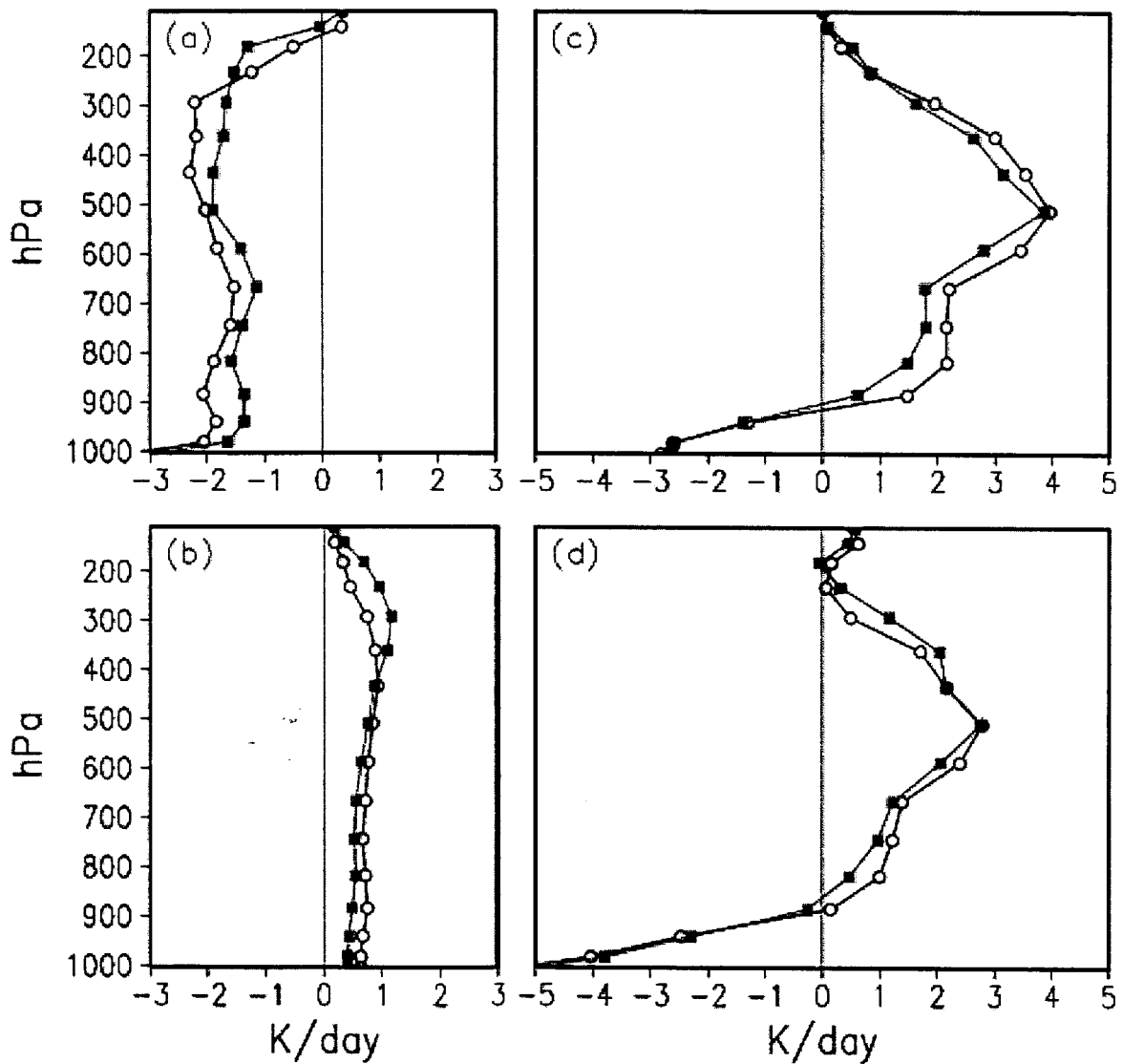


Figure 6 Joint distribution of maximum detrainment level and rain rate for E0. Warm-rain and cold- rain, and mixed-phase regions are as shown. Contours are population counts in natural logarithm scale.

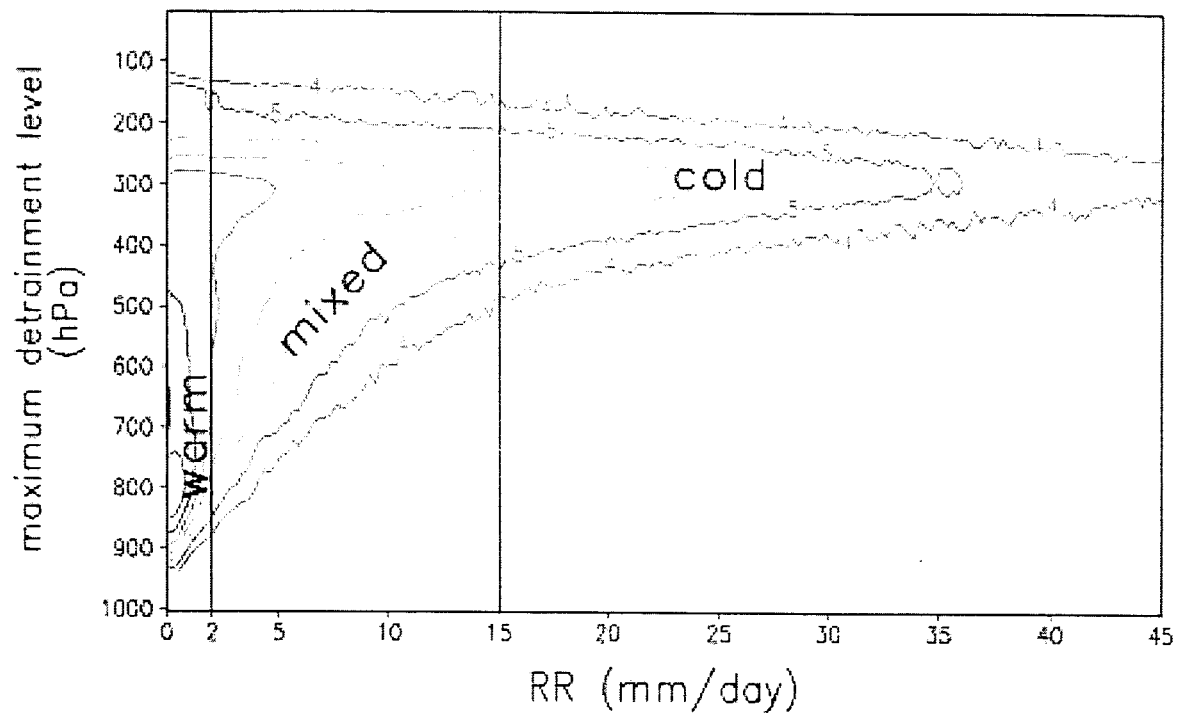


Figure 7 Vertical profile of E1-minus-E2 difference in Q, total heating (K/day); CL, cloudiness (percentage), and W, vertical velocity (negative hPa/day) for warm rain.

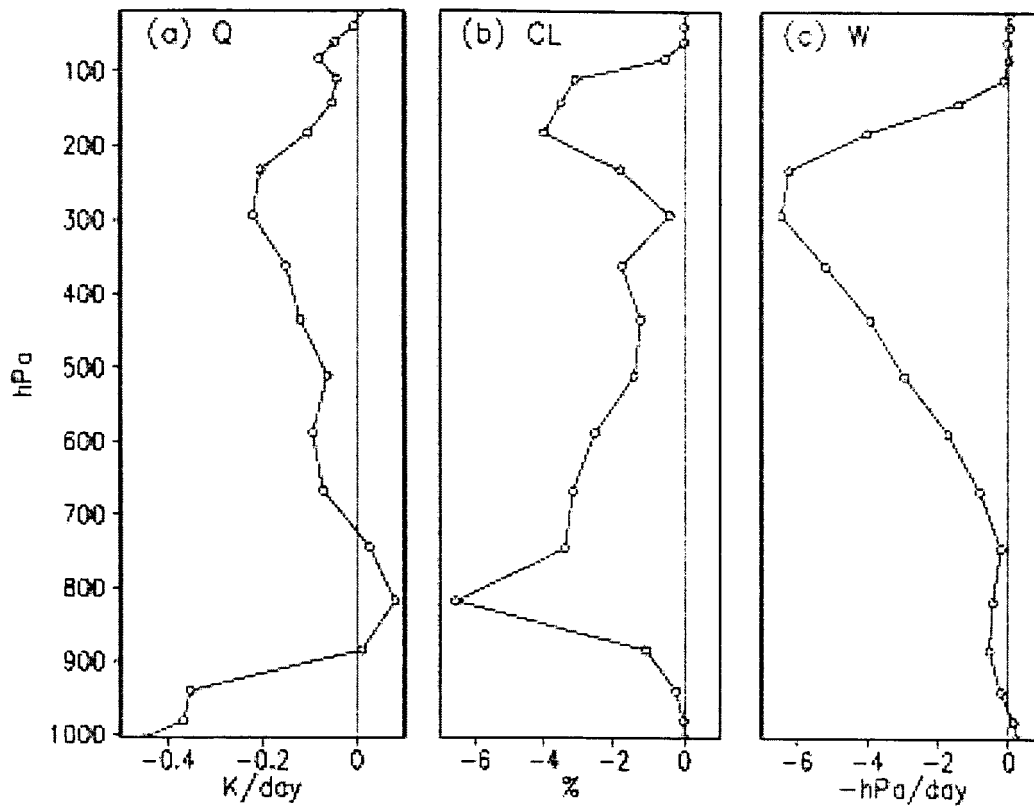


Figure 8 Same as in Fig. 6, except for cold rain.

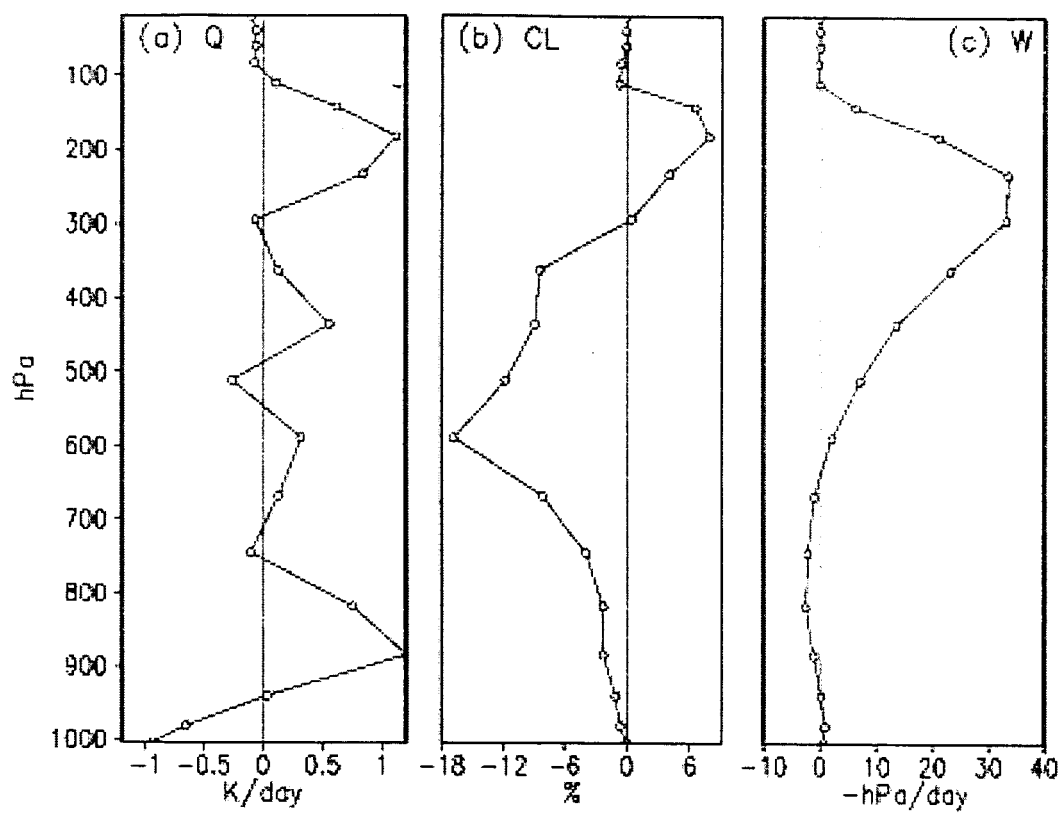


Figure 9 Longitudinal distribution of E1-minus-E2 difference in vertical mean p-velocity
(negative hPa/day) averaged over 20°S-20°N along the equator.

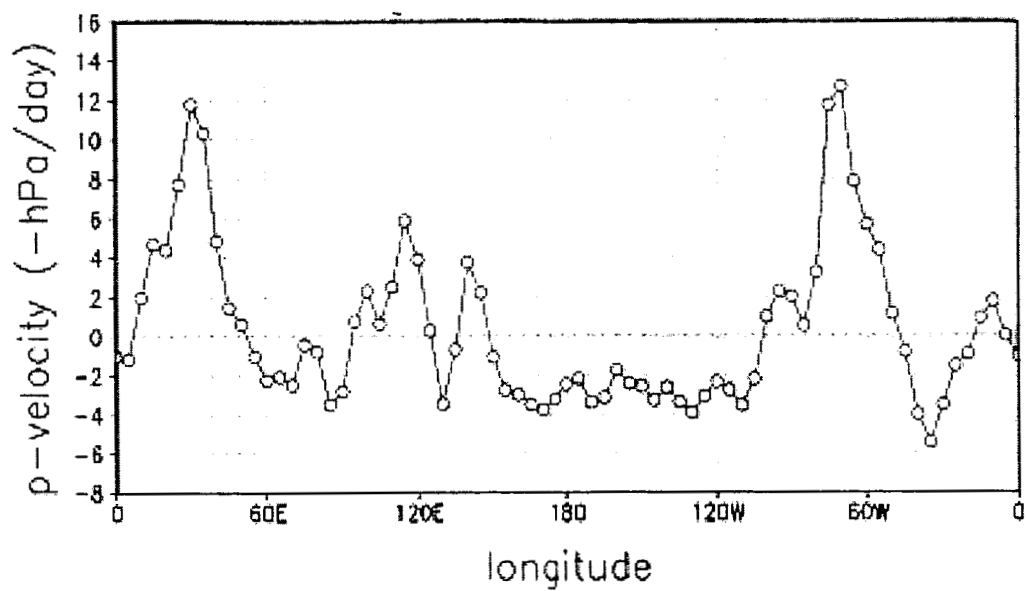


Figure 10 Height-longitude cross-section of E1-minus-E2 vertical velocity (negative hPa/day) averaged over 20° S - 20° N for a) the warm rain region, and b) the cold rain region. Vertical mean value has been subtracted.

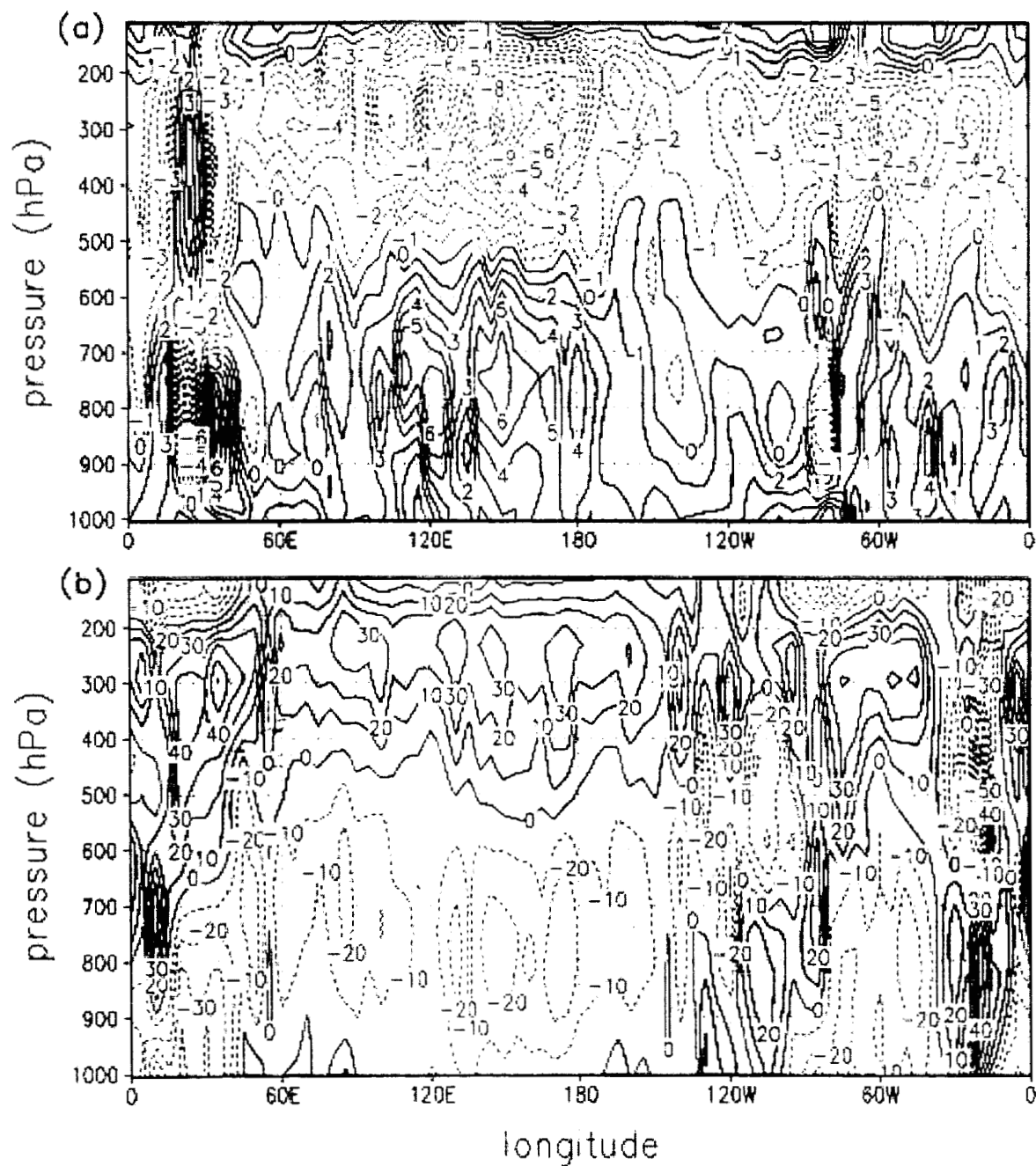


Figure 11 Height-longitude distribution of E1-minus-E2 temperature difference averaged over 20° S - 20° N. Units in °K. Vertical mean has been subtracted, and warm anomalies are shaded.

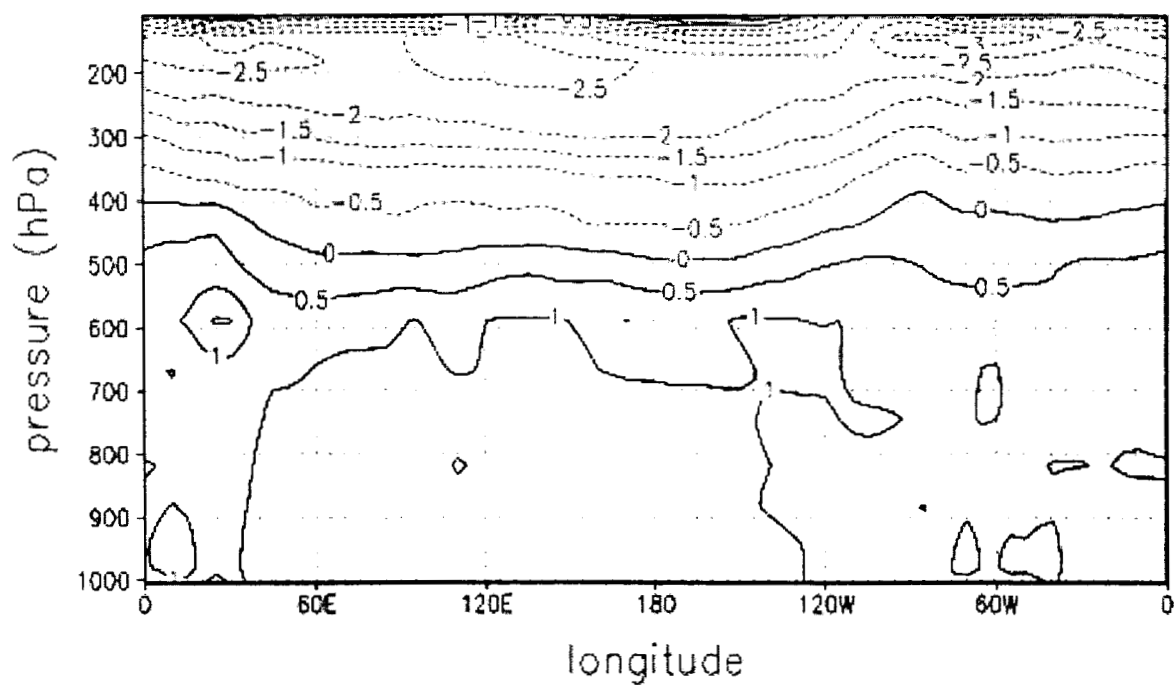


Figure 12 Height-time cross-sections of condensation heating over a) Indian ocean , b) western Pacific, c) central Pacific, and d) eastern Pacific for E1. Contours with heating greater than 1°K/day and 4°K/day are shaded.

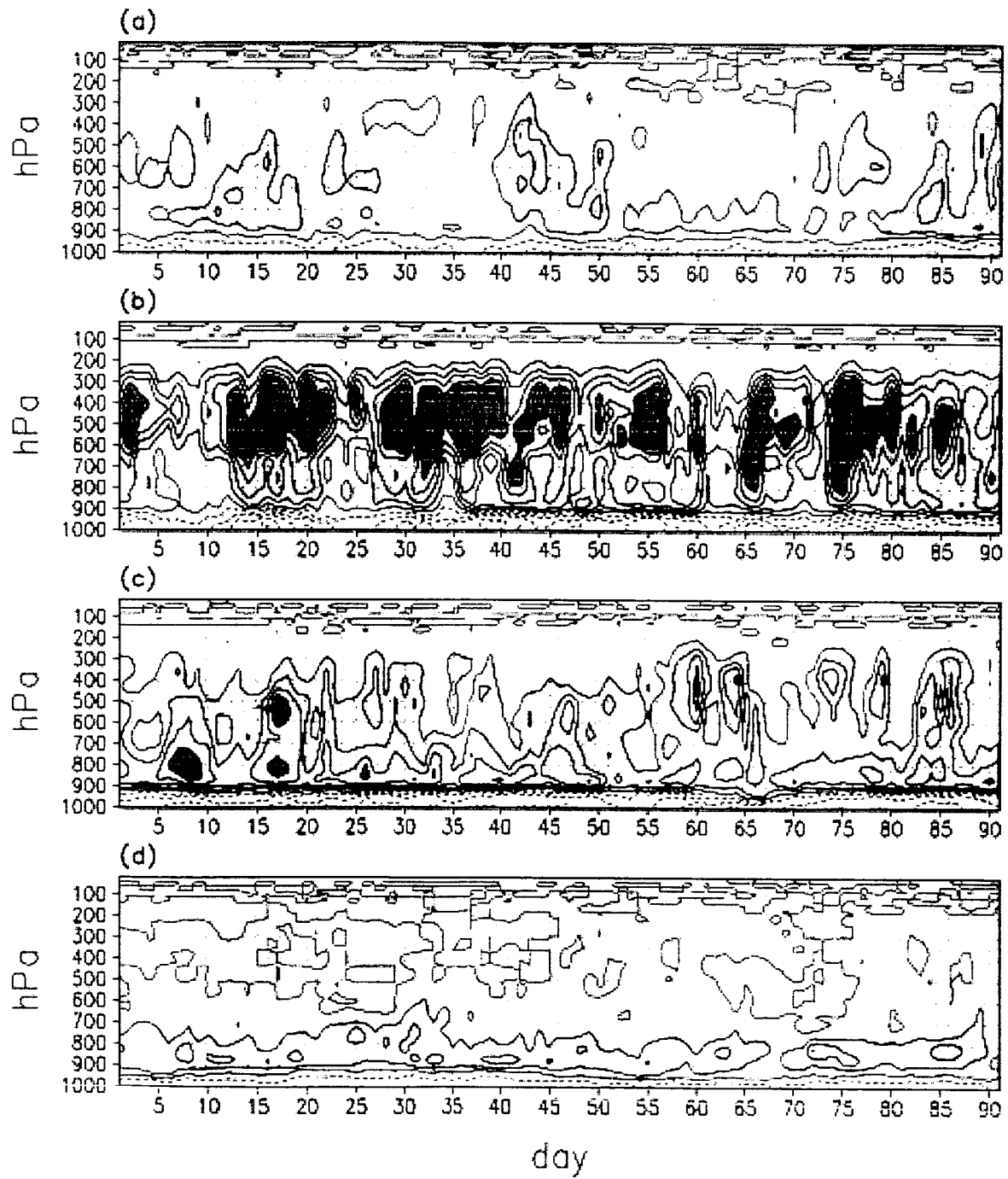


Figure 13 Same as in Fig. 12, except for E2.

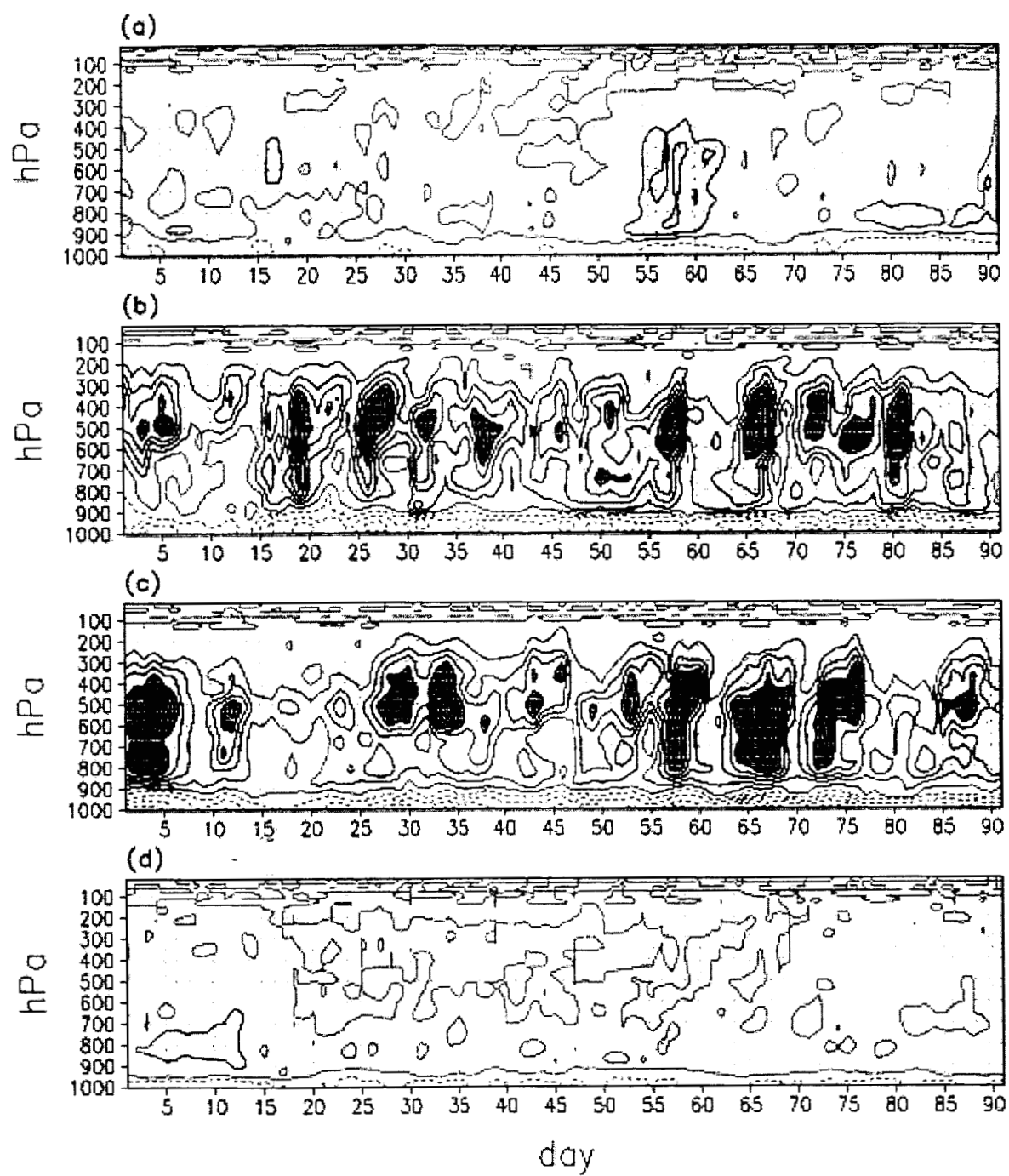


Figure 14 Spatial distribution of recycling time of deep convection for a) E1 and b) E2. Unit is in days. Areas with recycling time less than 15 and 10 days are shaded.

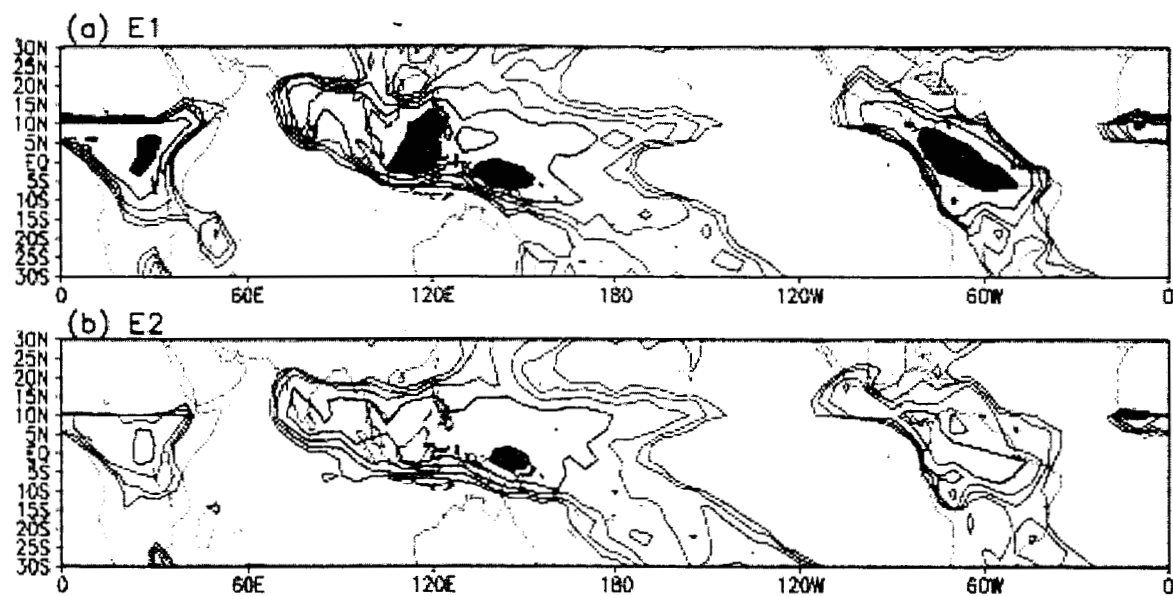


Figure 15 Height-time cross-section of detrainment rate over the western Pacific for a) E1 and
b) E2. Areas with detrainment rate greater than 2 and 4 kg/sec are shaded.

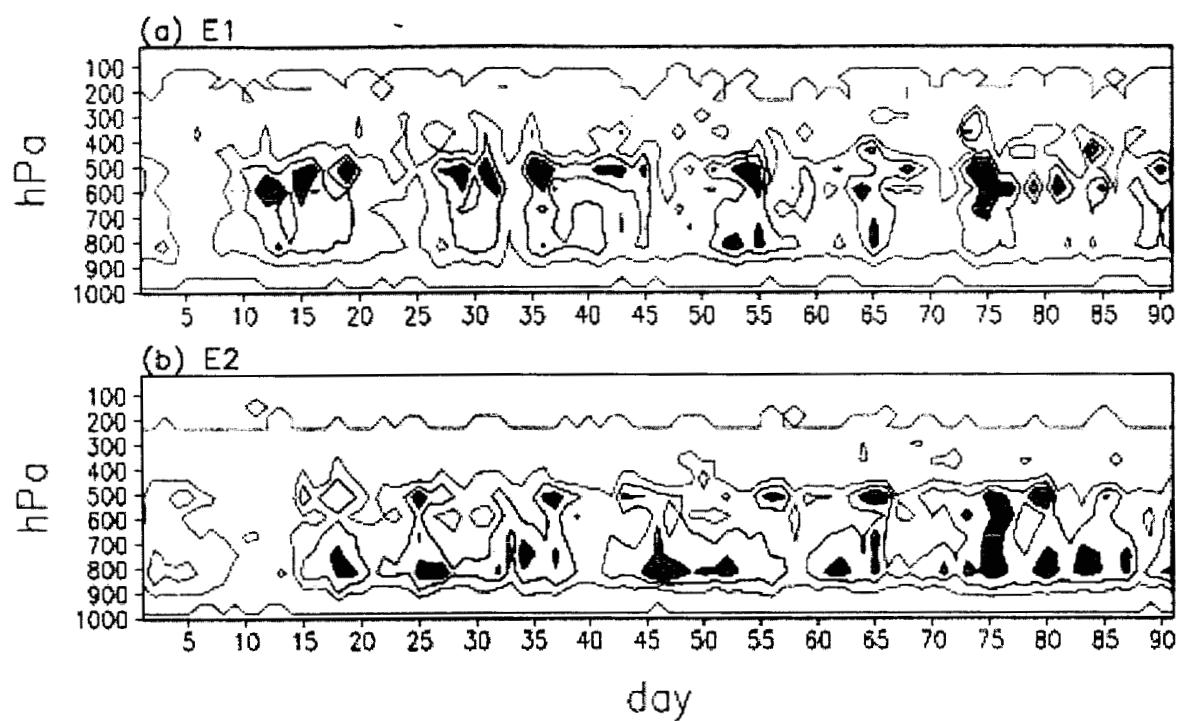


Figure 16 Time-longitude section of daily precipitation averaged along the equator (8° S - 8° N)
for a) E1 and b) E2. Unit is in mm/day.

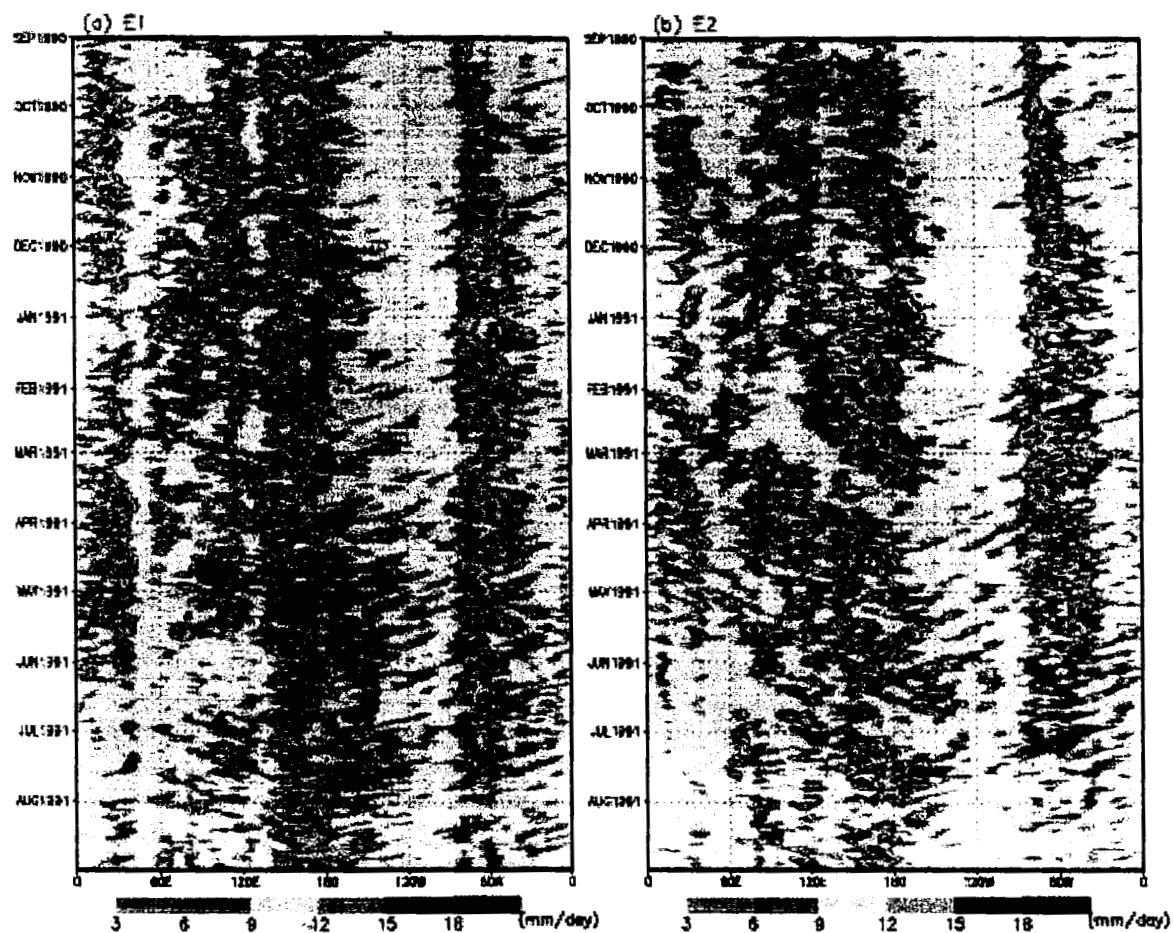


Figure 17 Same as in Fig. 16, except for OLR. Unit is in Wm^{-2} .

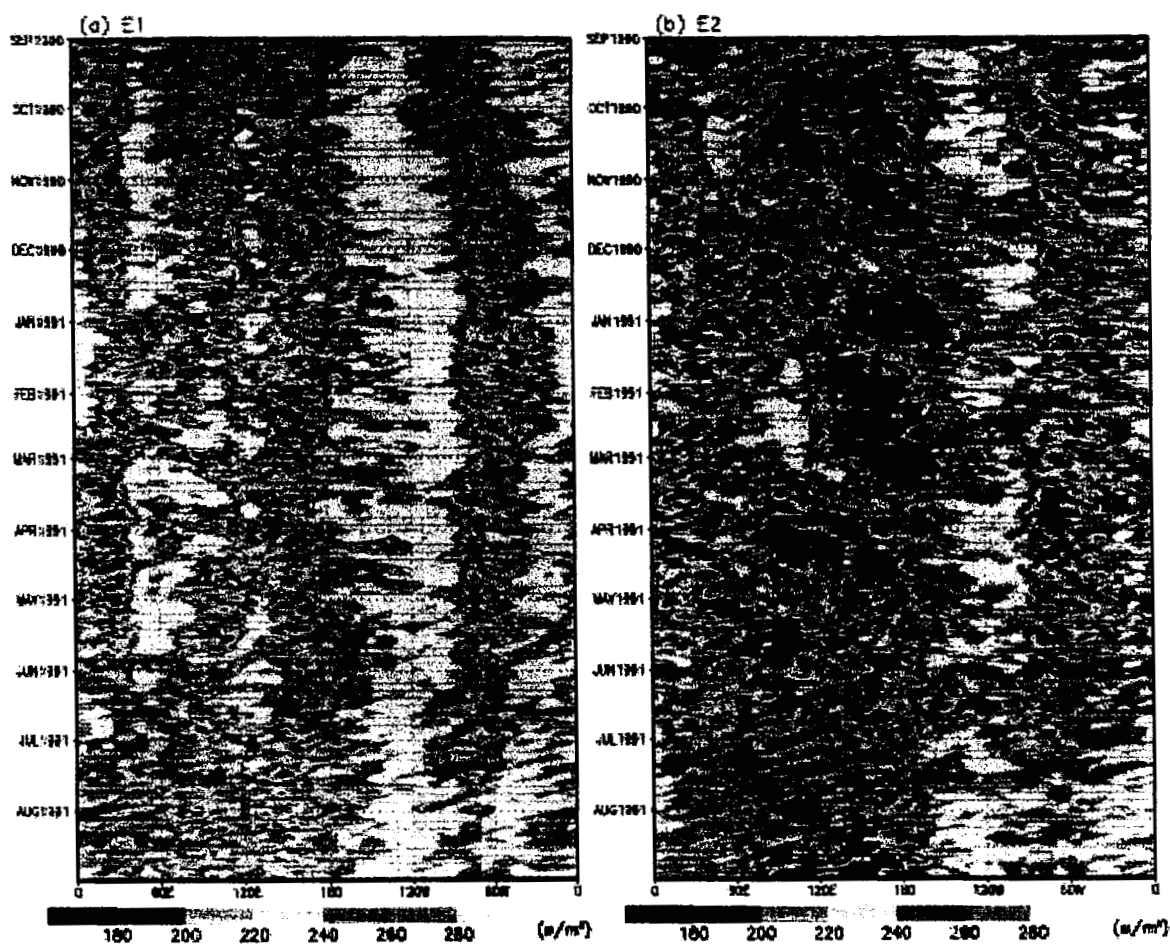


Figure 18 Spatial distribution of standard deviation of 20-70 day filtered precipitation for a) E1 and b) E2. Rain rates greater than 3 mm/day are shaded from light to dark.

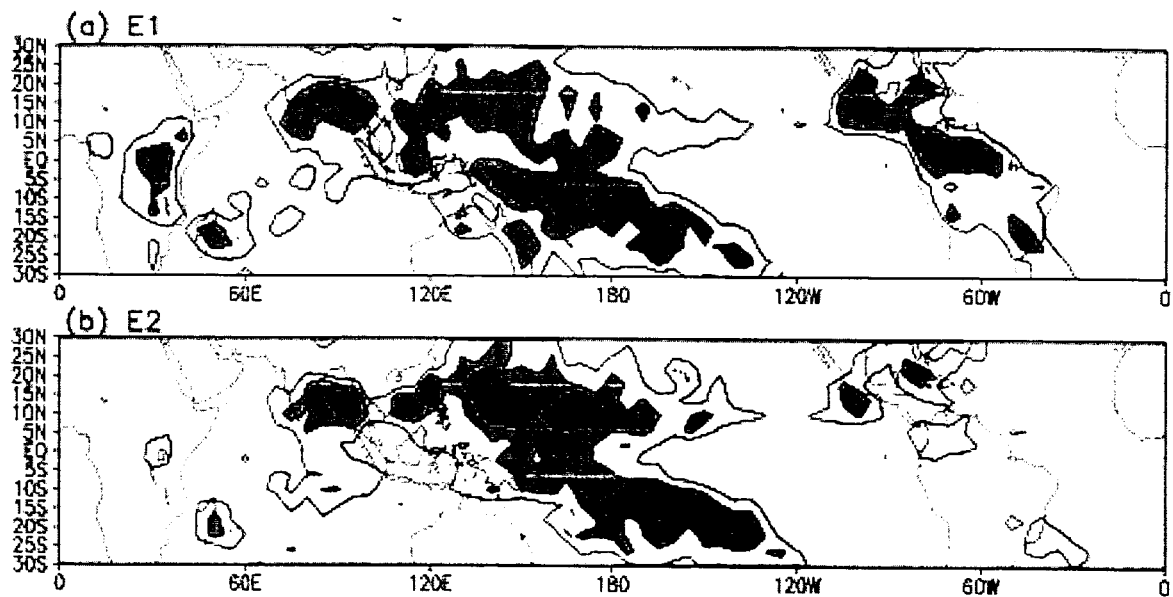


Figure 19 Time-longitude section of 20-70 day filtered 200 hPa velocity potential for a) E1 and b) E2. Units are in $10^6 \text{ m}^2 \text{ s}^{-1}$.

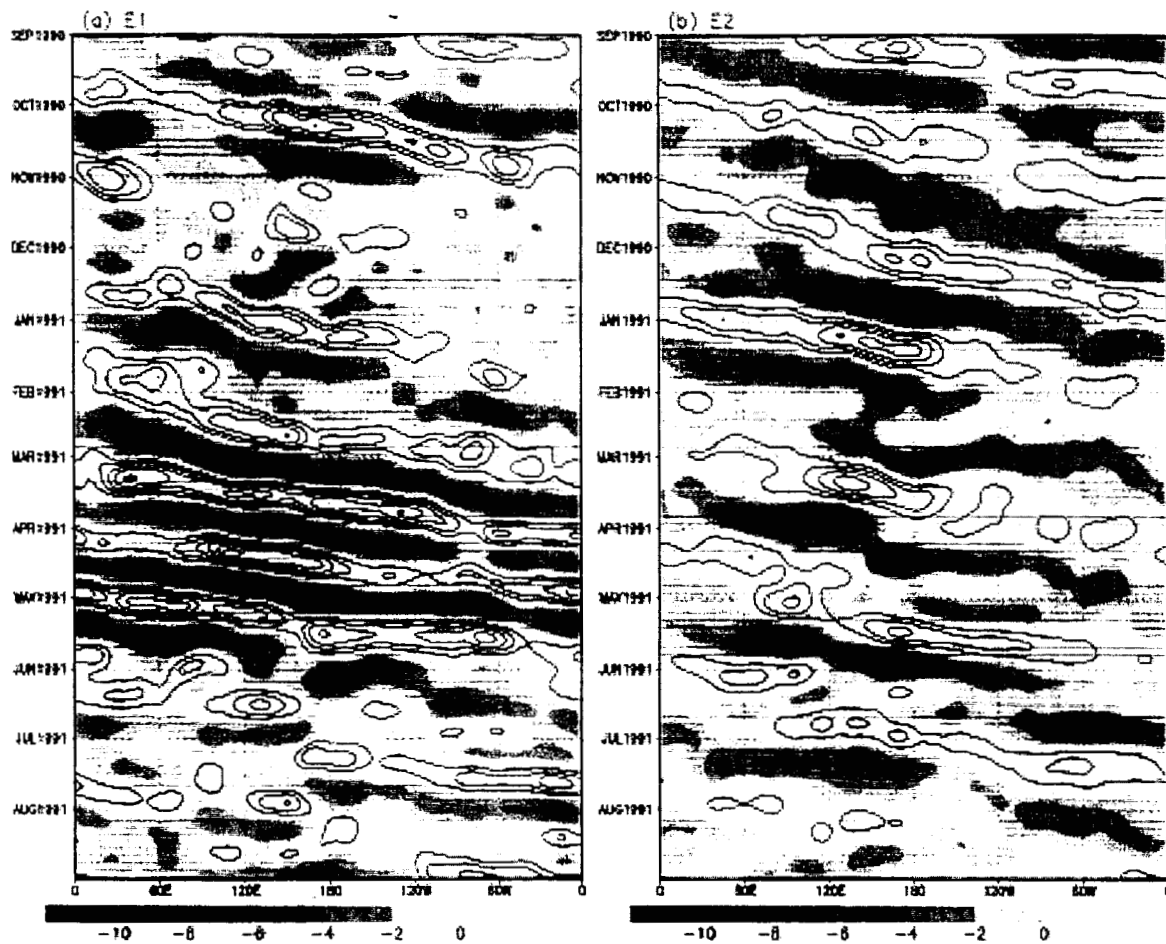


Figure 20 East-west wavenumber spectrum of 20-70 day filtered 200 hPa velocity potential for
a) E1 and b) E2.

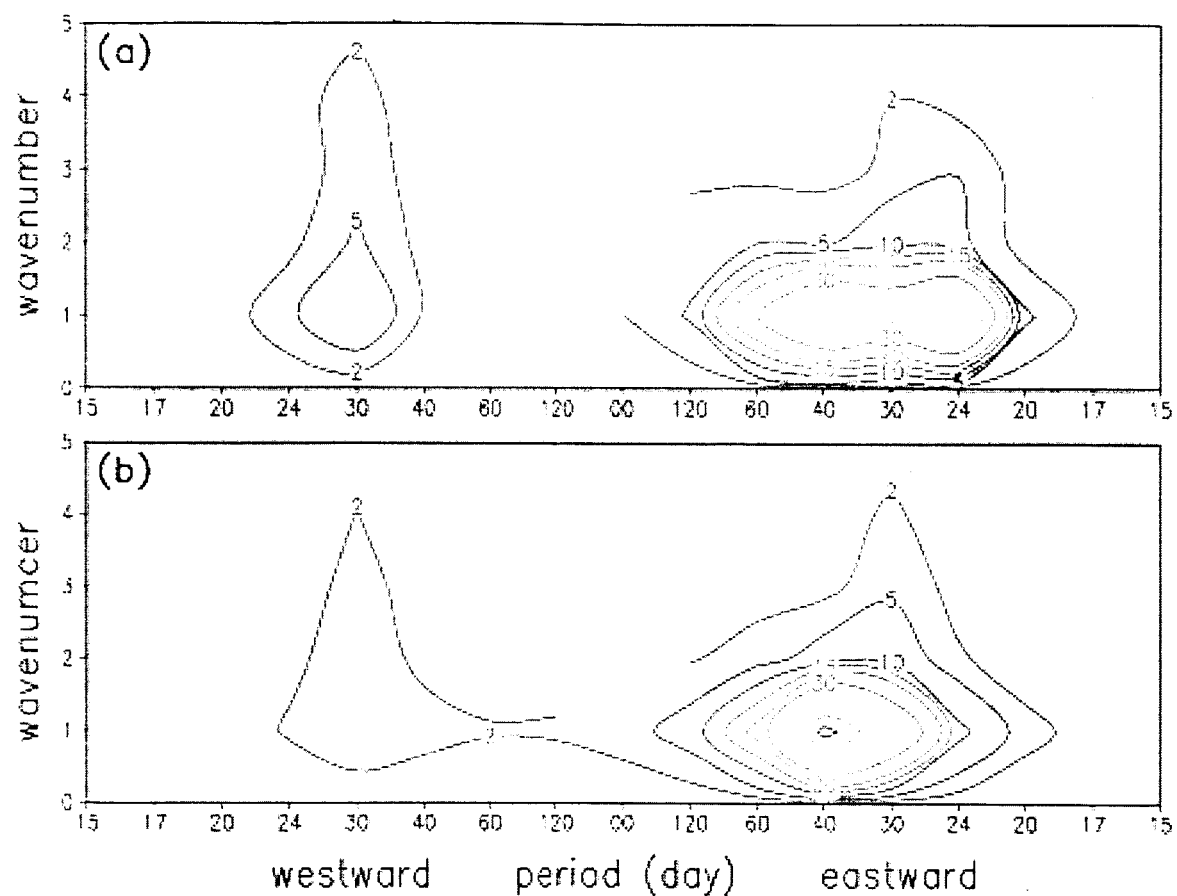


Figure 21 Schematic showing model predicted changes in the atmospheric hydrologic cycle, and cloud-radiative-dynamic feedbacks in the tropics due to increased autoconversion processes (see text for description).

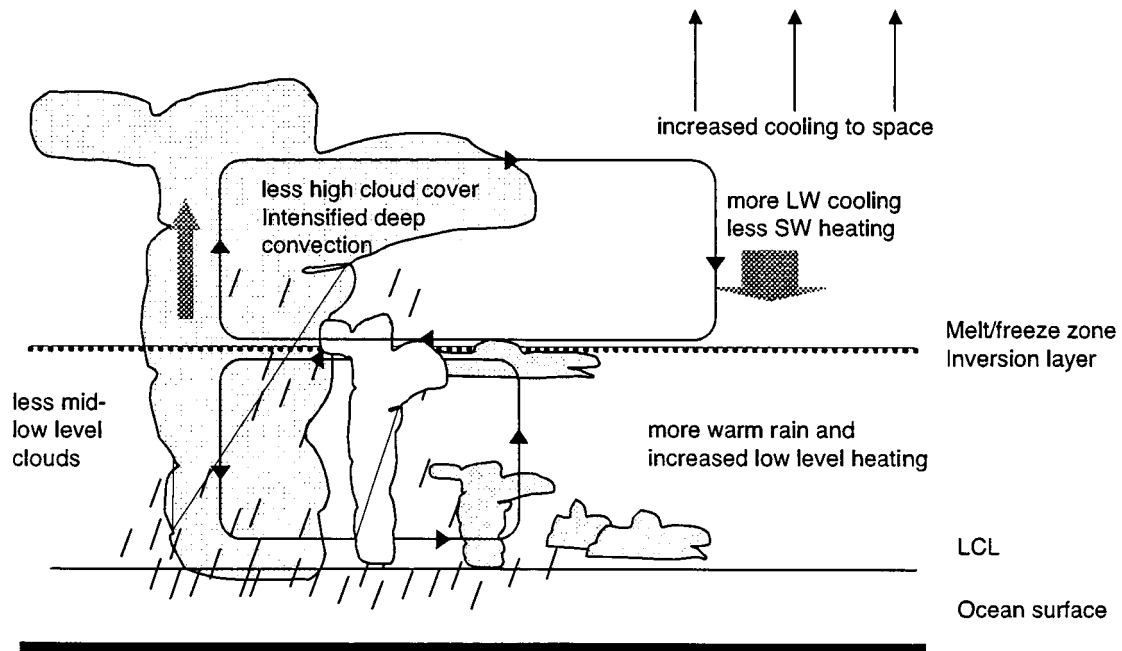


Fig. 21

Popular summary

The rate that a cloud loses its water to rain is known as the precipitation efficiency. According to a recent satellite observation study by GSFC scientists published in the *Journal of Geophysical Research Letters*, the efficiency of warm rain increases substantially as sea surface temperature rises, suggesting that the water cycle in the tropics is likely to accelerate in a warmer climate.

To better understand the response of the atmospheric water cycle to the increased warm-rain precipitation efficiency, we have used NASA's Goddard Earth Observing System (GEOS) atmospheric general circulation model to conduct climate simulations. We find that an increased rate of growth of cloud droplets to water drops produces more warm rain and less clouds at all heights due to rapid rainout. Fewer clouds cause increased longwave cooling and reduce shortwave heating in the upper troposphere, while increased warm rain enhances condensation heating in the lower troposphere. This vertical heating differential destabilizes the tropical atmosphere, producing a positive feedback resulting in more rain over the tropics.

The tropical circulation is very sensitive to radiative-dynamic effects induced by changes in precipitation efficiency. Reduced cloud-radiation due to an increased precipitation efficiency results in intermittent but more energetic eastward propagation of the Madden and Julian Oscillation (MJO). Conversely, a reduced precipitation efficiency, with increased cloud radiation produces MJO's with more realistic westward propagating transients, resembling a supercloud cluster structure. Our results suggest that warm rain and associated low and mid level clouds, i.e., cumulus congestus, may play a critical role in regulating the time-intervals of episodes of deep convections and hence the fundamental time scales of the MJO.

The implications of the present results on possible interactions of the atmospheric water cycle with aerosols and global warming are also discussed in this study.